

AD-A099 390

HUGHES RESEARCH LABS MALIBU CA  
CONTROLLED FIBER OPTIC SWITCHING.(U)  
DEC 80 O G RAMER

F/G 20/6

F33615-79-C-1864

UNCLASSIFIED

AFWAL-TR-81-1002

NL

1-1  
SEARCH



1-1



1-1

1-1

1-1

1-1

1-1



END  
DATE  
FILMED  
6-81  
DTIC

**LEVEL 1**

**P**  
SC

AFWAL-TR-81-1002



**AD A 099 390**

# CONTROLLED FIBER OPTIC SWITCHING

O.G. Ramer

Hughes Research Laboratories  
3011 Malibu Canyon Road  
Malibu, CA 90265

**S DTIC ELECTE D**  
MAY 27 1981  
C

December 1980

Contract No. F33615-79-C-1864

Final Report

For period 19 September 1979 through 1 October 1980

*Approved for public release; distribution unlimited.*

**DTIC FILE COPY**

X

AVIONICS LABORATORY  
AIR FORCE WRIGHT AERONAUTICAL LABORATORIES  
AIR FORCE SYSTEMS COMMAND  
WRIGHT-PATTERSON AFB, OHIO 45433


81 5 26 091


**NOTICE**

When Government drawings, specifications, or other data are used for any purpose other than in connection with a definitely related Government procurement operation, the United States Government thereby incurs no responsibility nor any obligation whatsoever; and the fact that the government may have formulated, furnished, or in any way supplied the said drawings, specifications, or other data, is not to be regarded by implication or otherwise as in any manner licensing the holder or any other person or corporation, or conveying any rights or permission to manufacture use, or sell any patented invention that may in any way be related thereto.


This report has been reviewed by the Office of Public Affairs (ASD/PA) and is releasable to the National Technical Information Service (NTIS). At NTIS, it will be available to the general public, including foreign nations.

This technical report has been reviewed and is approved for publication.

  
EUGENE R. NICHOLS, Project Engineer  
Electro-Optics Techniques and  
Applications Group  
Electro-Optics Technology Branch

  
KENNETH R. HUTCHINSON, Chief  
Electro-Optics Techniques and  
Applications Group  
Electro-Optics Technology Branch

FOR THE COMMANDER

  
WILLIAM J. EDWARDS, Chief  
Electronic Technology Division  
Avionics Laboratory

"If your address has changed, if you wish to be removed from our mailing list, or if the addressee is no longer employed by your organization please notify AFMIL/AADO-2 W-PAFB, OH 45433 to help us maintain a current mailing list".

Copies of this report should not be returned unless return is required by security considerations, contractual obligations, or notice on a specific document.

SECURITY CLASSIFICATION OF THIS PAGE (When Data Entered)

REPORT DOCUMENTATION PAGE		READ INSTRUCTIONS BEFORE COMPLETING FORM	
1. REPORT NUMBER <b>18</b> AFWAL TR-81-1002	2. GOVT ACCESSION NO. AD-A099390	3. RECIPIENT'S CATALOG NUMBER <b>9</b>	
4. TITLE (and Subtitle) CONTROLLED FIBER OPTIC SWITCHING		5. DATE OF REPORT & PERIOD COVERED Final Report 19 Sep 1979 - 1 Oct 1980	
7. AUTHOR(s) <b>10</b> O.G./Ramer		8. CONTRACT OR GRANT NUMBER(s) <b>15</b> F33615-79-C-1864 <i>new</i>	
9. PERFORMING ORGANIZATION NAME AND ADDRESS Hughes Research Laboratories 3011 Malibu Canyon Road Malibu, CA 90265		10. PROGRAM ELEMENT, PROJECT, TASK AREA & WORK UNIT NUMBERS 62204F <b>16</b> 2001 02169 <b>17</b> 02	
11. CONTROLLING OFFICE NAME AND ADDRESS Avionics Laboratory (AFWAL/AADO) Air Force Wright Aeronautical Laboratories Wright-Patterson AFB, OH 45433		12. REPORT DATE <b>11</b> Dec 1980	
14. MONITORING AGENCY NAME & ADDRESS (if different from Controlling Office)		13. NUMBER OF PAGES 94 <b>12</b> 34	
		15. SECURITY CLASS. (of this report) UNCLASSIFIED	
16. DISTRIBUTION STATEMENT (of this Report)  Approved for public release; distribution unlimited.		15a. DECLASSIFICATION DOWNGRADING SCHEDULE	
17. DISTRIBUTION STATEMENT (of the abstract entered in Block 20, if different from Report)			
18. SUPPLEMENTARY NOTES			
19. KEY WORDS (Continue on reverse side if necessary and identify by block number)  Fiber optics, Integrated optics, Fiber gyros, Switches <i>LP T...</i> <i>Delta-beta</i>			
20. ABSTRACT (Continue on reverse side if necessary and identify by block number)  This highly successful program has resulted in the demonstration of a low-loss, low-voltage, high-speed four-section <b>AB</b> -reversal switchable optical directional coupler which has been permanently coupled to single-mode fiber pigtails. The measured coupling losses between switch and fibers approach the measured optimum and theoretical predictions. In addition, experimental integrated-optic circuit			

**STIC  
ELECTRICAL  
MAY 27 1981**

170

SECURITY CLASSIFICATION OF THIS PAGE(When Data Entered)

(cont)  
L → losses, including waveguide bend, waveguide offsets, metal electrodes, and fiber-to-channel coupling, are presented. Coupling measurements from single-mode fiber to straight waveguides show losses less than 1 dB. Integrated-optic circuit losses due to waveguide bends and offsets were calculated and measured; these data are in excellent agreement. Although the overall loss of the delivered device is approaching theoretical limits, there are areas where obvious improvements are required, these areas are discussed in the recommendations and conclusions section of the report.

SECURITY CLASSIFICATION OF THIS PAGE(When Data Entered)

TABLE OF CONTENTS

SECTION		PAGE
1	INTRODUCTION AND SUMMARY . . . . .	9
2	COMPONENT DESIGN AND OPERATION PRINCIPLES . . . . .	13
	A. Switch Design . . . . .	13
	B. Fiber Attachment . . . . .	33
	C. Waveguide Losses . . . . .	48
	D. AR Coating Study . . . . .	55
	E. Outdiffusion Elimination Studies . . . . .	57
3	DELIVERABLE TEST RESULTS . . . . .	63
	A. Introduction . . . . .	63
	B. Program Goals and Results . . . . .	63
4	RECOMMENDATIONS AND CONCLUSIONS . . . . .	73
	A. Introduction . . . . .	73
	B. Fiber Coupler Fixture Optimization . . . . .	74
	C. Fiber-to-Waveguide Coupling @ 1.06 - 1.3 $\mu\text{m}$ . . . . .	75
	D. Switch Optimization for the Longer Wavelength . . . . .	76
	REFERENCES . . . . .	77
	APPENDIX - Analysis of Bends and Offset Losses in Integrated Optic Channel Waveguides . . . . .	79

Accession For	
NTIS GRA&I	<input checked="" type="checkbox"/>
DTIC TAB	<input type="checkbox"/>
Unannounced	<input type="checkbox"/>
Justification	
By _____	
Distribution/ _____	
Availability Codes	
Dist	Avail and/or Special
A	

LIST OF ILLUSTRATIONS

FIGURE		PAGE
1	Photograph of deliverable illustrating single mode fibers and switch . . . . .	10
2	Calculated conditions for electro-optically achieving a 3 dB (50/50) coupler . . . . .	15
3	Theoretical switching diagram for 1, 2, 3, 4 and 6 section switches operating in $\Delta\beta$ reversals . . . . .	17
4	Photograph of the $\Delta\beta$ reversal switch with 3-mm guides . . . . .	19
5	Experimental switch performance in both the conventional and $\Delta\beta$ reversal configuration . . . . .	19
6	Diffusion temperature cycle for waveguide formation . . . . .	24
7	Coupling length versus wavelength for uniform rectangular guides . . . . .	26
8	(a) Top view of a waveguide directional coupler where L is the coupler length, a is the waveguide width, and d is the separation between the waveguides in the interaction region . . . . .	28
	(b) Coupling coefficient of Ti-diffused LiNbO <sub>3</sub> waveguides at 1.06-, 0.83-, and 0.633- $\mu$ m wavelengths as a function of waveguide separation . . . . .	29
9	Method for determining the coupling coefficient, $\kappa$ . . . . .	30
10	Experimental data determining the coupling coefficient at 1.15 $\mu$ m wavelength for waveguides 5 $\mu$ m wide and 3 $\mu$ m gap . . . . .	31
11	Schematic of the four-port optical switch module . . . . .	34
12	Photograph of deliverable illustrating single mode fibers and switch . . . . .	35

FIGURE		PAGE
13	Photograph of the polished end of Si wafer with V grooves containing single mode fibers . . . .	36
14	The geometric aspect ratio of an isotropically diffused channel waveguide plotted versus the ratio of the undiffused channel width W to the diffusion length D. . . . .	39
15	Plotted in (a) is the ratio of the modal aspect ratios to the geometric aspect ratio for the first-order mode in several diffused channel waveguides . . . . .	40
16	Coupling coefficients associated with Gaussian beams . . . . .	41
17	(a) Variation in insertion ratios versus axial displacement (a) along the y direction, (b) along the z direction, and (c) along the x direction . . . . .	44
	(b) Variation in insertion ratios versus angular misalignments (a) horizontally and (b) vertically . . . . .	45
18	Schematic of the fiber-to-chip coupling loss measurement technique . . . . .	47
19	Coupling loss between ITT single mode fibers and Ti diffused strip waveguides of different widths for different diffusion times and Ti depths . . . . .	47
20	Photograph of a polished edge of a $\text{LiNbO}_3$ chip with Ti-diffused waveguides . . . . .	49
21	Sources of additional losses in integrated optics circuits related to mask making accuracy . . . . .	49
22	Calculated transmission through a waveguide bend formed by the intersection of two straight waveguides . . . . .	51
23	Calculated transmission through a waveguide discontinuity formed by a slight lateral displacement . . . . .	51



FIGURE		PAGE
24	Two section $\Delta\beta$ reversal switch operation at 60 Hertz . . . . .	52
25	Equivalent circuit model of $\text{LiNbO}_3$ -buffer layer electrode configuration . . . . .	54
26	Four section switch operation at 60 Hertz . . . . .	54
27	AR coating design . . . . .	56
28	Schematic of experimental setup for the AR coating test . . . . .	59
29	Elimination of outdiffused waveguides . . . . .	59
30	Schematic diagram of a switch system . . . . .	65
31	Switching curves for the deliverable shown are the drive voltage at 50 V/ division and the output of the two channels . . . . .	65
32	Experimental data showing the rise and fall time of the delivered switch and pulsed operation varying between (a) 2 $\mu\text{sec}$ ; (b) 4 $\mu\text{sec}$ ; (c) 500 $\mu\text{sec}$ . . . . .	67
33	Experimental data showing optical amplitude pulse drift . . . . .	69
34	Photograph of deliverable illustrating single mode fibers and switch . . . . .	71

## SECTION 1

### INTRODUCTION AND SUMMARY

Guided-wave optical circuits composed of integrated optical (IO) and fiber optic (FO) devices are a rapidly emerging communication and signal processing technology that offers very large bandwidths while being immune to interference and crosstalk. In this program, we have designed, fabricated, tested, and delivered to the Air Force an electrically activated planar waveguide switch, one of the key IO components required to implement signal-processing concepts. This four-port planar device packaged with single-mode fiber-optic pigtailed is shown in Figure 1. Applications of the device include signal processing for interferometric sensors such as fiber-optic rotation sensors<sup>1</sup>(FORS) and programmable tapped delay lines to synthesize transversal filters in electronic warfare systems.

The switch development was divided into two phases: chip development (involving the development of the IO chip with the 2 x 2 switch) and fiber-to-chip interfacing (involving the permanent coupling of single-mode fiber-optic pigtailed to the four ports of the chip). The theory and design involved in these phases are described in detail in Section 2. Briefly, the switch format was based on coherent coupling between waveguides formed in Z-cut LiNbO<sub>3</sub>. The control of the coupling was achieved by electro-optically varying the phase propagation constants of each guide. The electrode arrangement divides the coupler into four equal-length sections, such that the  $\Delta\beta$  reversal<sup>2</sup> technique could be used to achieve both the bar state (straight through propagation) or the cross state.

Specific accomplishments made during this program in chip development include

- Demonstration of a four-section  $\Delta\beta$  reversal switch at 0.85  $\mu\text{m}$  wavelength.
- Identification and verification of additional on-chip losses associated with waveguide bends and small offsets or displacement of one waveguide section with respect to another.

10353-13



Figure 1. Photograph of deliverable illustrating single mode fibers and switch.

- Experimental demonstration of  $\text{Li}_2\text{O}$  out-diffused mode elimination.
- Buffer layer deposition to eliminate losses caused by the electrodes.

The second technical area, fiber-to-chip interfacing, required the development of appropriate fixturing and manipulation techniques to achieve the close tolerance requirements for high coupling efficiency between a fiber with an  $\sim 5\text{-}\mu\text{m}$  core and a channel guide with roughly a  $2\text{-}\mu\text{m}$  by  $5\text{-}\mu\text{m}$  cross section. Specific accomplishments made in this area during this program include:

- Demonstration of better than 1-dB coupling between single-mode fiber and channel-diffused waveguide.
- Development of a coupling fixture and polishing techniques that are close to achieving the required tolerances necessary to permanently couple single-mode fiber to diffused channel waveguides with losses limited by fundamental considerations.
- Fabrication of a deliverable switch with 2-dB losses between fiber and chip (total loss 7.8 dB).

Section 2 presents the component design and operation principles for the switch and fiber-to-chip coupling. In addition, Section 2 contains much of the preliminary experimental data associated with the switch optimization; this includes data on single-mode fiber-to- $\text{LiNbO}_3\text{:Ti}$  diffused waveguide coupling, switch optimization using the optimum waveguide for fiber-to-waveguide coupling, buffer layers between electrodes and waveguides, AR coatings, and fiber coupler fixture.

Section 3 explains in detail the performance of the delivered item versus the SOW requirements. In summary, the device had the following characteristics.

- Four-section  $\Delta\beta$  reversal switch with  $\text{SiO}_2$  buffer layers attached to four single-mode fiber pigtails. Wavelength of operation is  $83\ \mu\text{m}$ .
- Total throughput loss was 7.8 dB; this is  $\sim 2.4$  dB larger than fundamental limitations.

- Crosstalk between channels of  $\sim 20$  dB.
- No AR coatings between fibers and chips resulted in reflections from chip edges
- Switch exceeds all pulse requirements for on and off times. The operational bandwidth of the switch is  $\sim 100$  Hz to 500 MHz.
- Switches of this kind can be made in the wavelength ranges of 1.06 to 1.3  $\mu\text{m}$ . Recently, a 1.06- $\mu\text{m}$  switch was demonstrated at HRL.

Section 4 outlines the technology development required for significant performance improvement of the IO chip and operation in the wavelength region of 1.06 to 1.3  $\mu\text{m}$ . The areas where additional research are recommended are:

- Deposition of AR coatings on chip edges
- Development of buffer layers that will allow switch operation at dc
- Elimination of  $\text{Li}_2\text{O}$  out-diffusion mode problems to optimize the switching voltages
- Optimization of fiber coupler fixture
- Optimization of fiber-to-waveguide coupling at longer wavelengths
- Optimization of switches with the optimum waveguides and electrode arrangement at longer wavelengths.

## SECTION 2

### COMPONENT DESIGN AND OPERATION PRINCIPLES

#### A. SWITCH DESIGN

##### 1. Switch Operation

The operation of the directional coupler switch is based on the coherent exchange of radiation between two single-mode channel waveguides of width  $W$  placed in close proximity (i.e., separated by a gap  $G$ ) and configured so as to run parallel over an interaction length  $L$ . The waveguide patterns are formed in  $\text{LiNbO}_3$  by diffusion of Ti with thickness  $d$ . An electrode arrangement divides the coupler into equal-length sections in which voltages of equal or opposite sign can be applied to electro-optically (Pockels effect) control the phase propagation constants of each guide. With equal magnitude and opposite voltages applied to alternating sections, a propagation constant mismatch  $(\beta_1 - \beta_2) = \Delta\beta$  is imposed in half of the switch, and  $-\Delta\beta$  is imposed in the other half.

The manner in which a light beam couples its energy back and forth between two parallel dielectric channels can be completely characterized by three parameters:  $L$ ,  $\Delta\beta$ , and  $\kappa$ . The parameter  $\kappa$  is a measure of the strength of the interchannel coupling. The physical interpretation of  $\kappa$  is simplified by considering the situation  $\Delta\beta = 0$ ; in this case, the distance  $\ell$  over which 100% power transfer occurs is given by  $\Delta\beta = \pi/2\kappa$ . In the single-electrode switch designs of a directional coupler, the transfer is controlled by spoiling the conditions of  $\Delta\beta = 0$  and  $\ell = \pi/2\kappa$ . For optimum operation, the device must have a length equal to  $n\ell$ , where  $n$  is an odd integer. The exact attainment of both  $\Delta\beta = 0$  and  $L = \pi/2\kappa$  makes fabrication of a 100% transfer device very difficult. These requirements are relaxed by using the  $\Delta\beta$ -reversal configuration developed by Schmidt and Kogelnik.<sup>2</sup>

The switching action can be modeled by solving the coupled-mode equations

$$R' - j\delta R = j\kappa S$$

$$S' + j\delta R = j\kappa R \quad ,$$

where  $\delta \equiv (\beta_1 - \beta_2)/2$ , and the primed quantities refer to the spatial derivative  $d/dz$  ( $z$  being the direction of propagation). For a single section electrode, the solutions written in matrix form for arbitrary input amplitudes  $R_0$  and  $S_0$  and device length  $z = L$  are

$$\begin{bmatrix} R \\ S \end{bmatrix} = \begin{bmatrix} A_1 & -jB_1 \\ -jB_1^* & A_1^* \end{bmatrix} \begin{bmatrix} R_0 \\ S_0 \end{bmatrix}$$

where

$$A_1 = \cos \left( z (\kappa^2 + \delta^2)^{1/2} \right) + j\delta \sin \left( z (\kappa^2 + \delta^2)^{1/2} \right) / (\kappa^2 + \delta^2)^{1/2}$$

$$B_1 = \kappa \sin \left( z (\kappa^2 + \delta^2)^{1/2} \right) / (\kappa^2 + \delta^2)^{1/2}$$

$$\delta = \Delta\beta/2 \quad .$$

A device in this configuration can be used effectively as a controllable 50/50 beam splitter by adjusting the length,  $L$ , such that  $B_1^2 (\delta = 0) = \sin^2 KL \geq .5$  or  $L > \ell/2$ . The control comes by adjusting  $\delta$  (applying an electric field) such that  $B_1^2 = .5$ . This condition is plotted in Figure 2.

10353-12

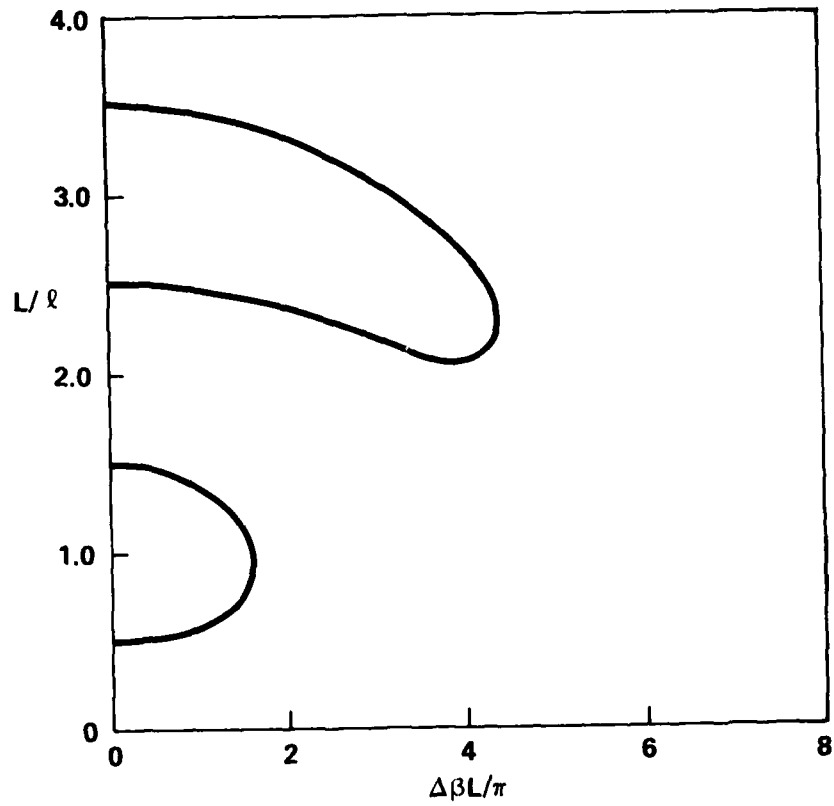


Figure 2. Calculated conditions for electro-optically achieving a 3 dB (50/50) coupler.



For the two-section  $\Delta\beta$  reversal switch shown in Figure 3, the solutions written in matrix form are for arbitrary input amplitudes  $R_o$  and  $S_o$  and device length  $2Z = L$ ,

$$\begin{bmatrix} R \\ S \end{bmatrix} = \begin{bmatrix} A_2 & -jB_2 \\ -jB_2^* & A_2^* \end{bmatrix} \begin{bmatrix} R_o \\ S_o \end{bmatrix} = \begin{bmatrix} A_1^* & -jB_1 \\ -jB_1^* & A_1 \end{bmatrix} \begin{bmatrix} A_1 & -jB_1 \\ -jB_1^* & A_1^* \end{bmatrix} \begin{bmatrix} R_o \\ S_o \end{bmatrix}$$

-  $\delta$  section    +  $\delta$  section

where

$$A_2 = 1 - 2B_1^2$$

$$B_2 = 2A_1^* B_1$$

Assuming initial conditions with  $(R_o, S_o) = (1, 0)$ , corresponding to all power being initially in one guide, zero crosstalk in the crossed or parallel states is assured by setting  $A_2 = 0$  and  $B_2 = 0$ , respectively. Each of these conditions establishes a correspondence between the normalized parameters  $L/\ell$  and  $\Delta\beta/L$ ; this correspondence is plotted in Figure 3b. The interpretation of this switch diagram is straightforward. If  $L/\ell$  is between 1 and 3, there exist values of  $\Delta\beta$  (a function of the applied voltage or electric field under the electrodes) that will drive the device onto both the parallel and crossed curves. Thus, device length is a noncritical parameter, just as it is in a single-electrode switch. Switch diagrams for 1, 2, 3, 4, and 6 electrodes or sections are shown in Figures 3(a) through 3(e), respectively. The work performed to date has been concentrated on the switch designs with two and four sections. The wavelengths of operation have been  $6328 \mu\text{m}$ ,  $.83 \mu\text{m}$ ,  $1.06 \mu\text{m}$ . At  $.8 \mu\text{m}$ , a four-section switch configuration resulted in

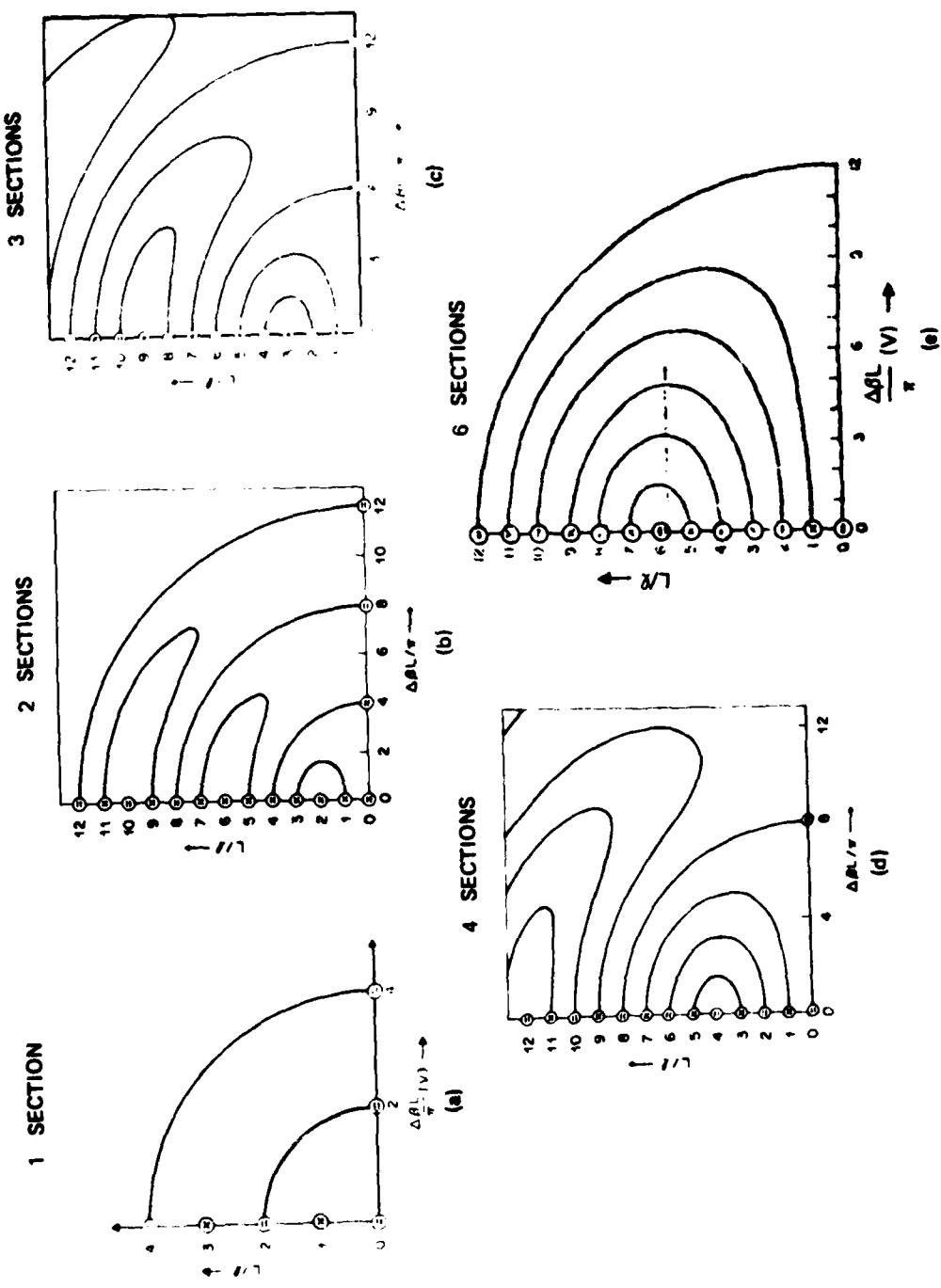


Figure 3. Theoretical switching diagram for 1, 2, 3, 4, and 6 section switches operating in  $\Delta\beta$  reversals.

reduced switch voltages of 11 volts for the cross state and 22 volts for the straight through state. These voltages are approximately half the switch voltage for the two section switch. Hence, the advantage of longer devices and more sections.

As an example, we present here some of the results we obtained with the 0.6328- $\mu\text{m}$  switch with two sections. The switch electrodes and guides are shown in Figure 4. The light intensities in the two channels measured at 0.6328  $\mu\text{m}$  wavelength versus the applied voltages are shown in Figure 5. Complete crossover and straight-through states have been achieved with 25- to 30-dB isolation. The variation from sample to sample, we believe, is caused by misalignment of the electrodes with the guide structure. The asymmetry of the switching characteristics with voltage is due mainly to the electrode misalignment and optical damage. Figure 5(a) shows the device operation with the same voltage applied to the split electrodes. The straight-through, =, state is attained in this way. Figure 5(b) shows the device operation in the AB-reversal mode to attain complete crossover.

## 2. Linear Electro-optic (Or Pockels) Effect

Electro-optic effects may be broadly defined to include changes in index of refraction, changes in absorption (electro-absorption), and changes in scattering caused by the application of an electric field to a material through which light is propagating. We will mainly discuss refractive index changes induced by electric fields. If the index change varies linearly with the amplitude of the applied field, the effect is known as the linear electro-optic, or Pockels, effect.

As explained by Nye,<sup>3</sup> the Pockels effect is observed only in crystalline solids that lack a center of symmetry. At present, the Pockels effect is the most widely used of the physical effects for constructing light modulators.

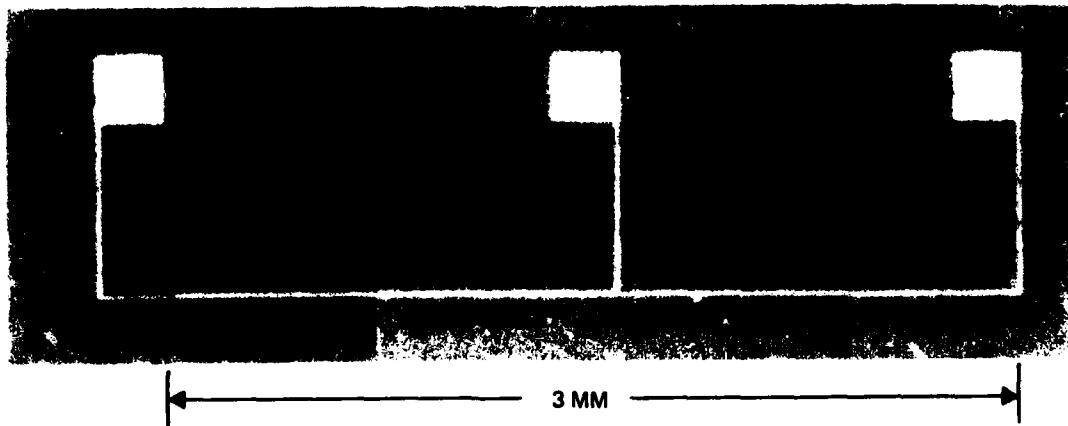


Figure 4. Photograph of the  $\Delta\beta$  reversal switch with 3-mm guides. The electrodes are 4- $\mu\text{m}$  wide with 3-mm spacing. The switch length is 3-mm.

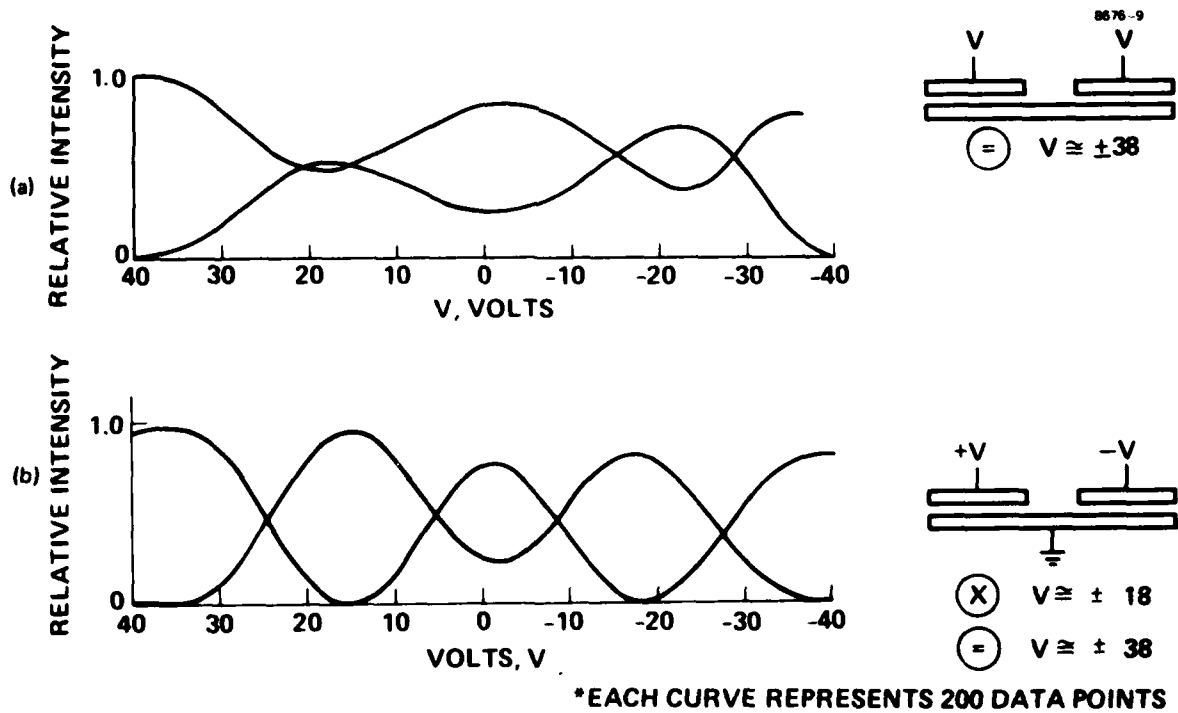


Figure 5. Experimental switch performance in both the conventional (a) and  $\Delta\beta$  reversal (b) configuration.

The magnitude of the linear electrooptic effect is calculated by using the electrooptic coefficients that relate the changes in refractive index to the amplitude of the applied electric field. The electrooptic coefficients are the elements of a third-rank tensor which interrelates the applied field and light polarization and propagation directions referred to the crystalline axes to the index changes.

Nye<sup>3</sup> gives a detailed description of the meaning and use of the electrooptic tensor. This work is summarized below.

The refractive index of a general crystalline material is specified by the indicatrix or index ellipsoid. The intersection of a plane passing through the center of the index ellipsoid with the ellipsoidal surface is an ellipse. The length  $B_i$  of one of the two principal axes of this ellipse is related to the index of refraction  $n_i$  of light propagating in a direction normal to the plane and linearly polarized parallel to that principal axis by  $n_i = 1/\sqrt{B_i}$ . Light propagating normal to the plane but polarized at an angle parallel to neither principal axis propagates as two waves with velocities (refractive indices) corresponding to the reciprocal square roots of the lengths of the two principal axes and with amplitudes proportional to the cosines of the angles between the polarization direction and the direction of the principal axes.

The linear electrooptic effect can be described by small changes in the size and orientation of the indicatrix caused by an applied field. Since the Pockels effect is very small ( $\Delta n \sim 10^{-4}$ ), for most purposes rotational effects on the indicatrix can be neglected and the significant changes described through variations in the length of the principal axes of the index ellipsoid.

Crystals that show the linear electrooptic effect are also piezoelectric. Piezoelectricity is an electric-field-induced stress. This is important because stress variations also produce changes in refractive index through the photoelastic effect. Thus, to correctly describe the

total index change that takes place when an electric field is applied, it is necessary to prescribe the mechanical constraints placed on the crystal. This is done by specifying the electrooptic coefficients for either the clamped or unclamped conditions. The clamped condition corresponds to a crystal under constant strain and is applicable to situations in which the frequency of the modulating field is well above mechanical crystal resonances. In the unclamped (free) condition, the crystal is under zero stress and the coefficients so specified are used for frequencies well below the mechanical resonances. Thus, generally the clamped coefficients are used for high frequencies and the unclamped coefficients are used for low frequencies.

For linear polarized light propagating perpendicular to a principal plane of the index ellipsoid, the electrooptic refractive index change may be expressed as

$$\Delta n = \frac{-n'^3 r' E}{2} ,$$

where  $n'$  is a linear combination of the principal refractive indices,  $r'$  is a linear sum of electrooptic coefficients, and  $E$  is the appropriate component of the applied electric field.

A summary of the use of the electrooptic tensor and tables of electrooptic coefficients were given by Kaminow in Ref. 4.

Because the linear electrooptic effect is basically due to electronic lattice transitions, the response time of the index change approaches the electronic lattice relaxation times, which are in the range  $10^{-13}$  to  $10^{-14}$  sec. Thus, for practical application, the frequency response of the linear electrooptic effect need hardly be considered.

In Table 1 are listed typical values of the electrooptic coefficient and refractive index for  $\text{LiNbO}_3$ ,  $\text{ZnO}$ , and  $\text{GaAs}$ . These are materials of technological importance which have been used for modulators.

Table 1. Some Typical Electrooptic Coefficients and Refractive Index Changes for Applied Fields of 10,000 V/cm

Relative Dielectric Constant	Material	$\lambda$ , $\mu\text{m}$	$n'$	$r'$ , $10^{-12}$ m/V	$\Delta n$ $E = 10^4$ V/cm
28	LiNbO <sub>3</sub>	0.6328	2.203( $n_e$ )	30( $r_{33}$ )	$1.6 \times 10^{-4}$
12.3	GaAs	0.9	3.6( $n$ )	1.2( $r_{14}$ )	$2.8 \times 10^{-5}$
8.2	ZnO	0.6328	2.015( $n_e$ )	2.6( $r_{33}$ )	$1.1 \times 10^{-5}$
Values of $n$ , $r$ , and $\epsilon$ from Ref. 4.					

7128

Values of  $\Delta n$  calculated from Ref. 4 when a field of  $10^4$  V/cm is applied are also listed. We note from Table 1 that, even with LiNbO<sub>3</sub>, which has one of the strongest electrooptic effects of commercially available materials, a field of  $10^4$  V/cm gives an index change of less than two parts in  $10^4$ .

### 3. Channel Waveguide Formation in LiNbO<sub>3</sub>

Low-loss single-mode optical channel waveguides are fabricated in LiNbO<sub>3</sub> substrates by the in-diffusion of titanium metal. The presence of Ti ions increases the polarizability of the medium, thus generating a region of higher index of refraction. By adjusting the thickness and the width of the Ti channel, single-mode optical waveguides in both the transverse and depth directions are easily obtained.

Photolithography techniques are used to define the Ti pattern. These techniques include sputter etching, chemical etching, and

photoresist lift-off. At HRL, the photoresist lift-off technique is used to form the desired Ti pattern because it provides a better edge definition of Ti channels. During the fabrication process, the pattern of single-mode channel waveguides are first delineated on the positive Shipley AZ 1305B photoresist. After exposing and developing the photoresist, a 200- to 600-Å-thick Ti film is electron-beam (E-beam) deposited onto the photoresist pattern for guides. The open area is thus filled with Ti metal. The unwanted Ti coating on the photoresist is removed by dissolving the photoresist underneath in acetone. The in-diffusion process is performed in a flowing oxygen atmosphere at a temperature between 900 and 1000°C. The diffusion time is 6-8 hrs. Before diffusion, the Ti metal is oxidized to TiO<sub>2</sub> at 600°C. The addition of the oxidation step before diffusion enhances the surface quality of the sample and the reproducibility of the diffusion process. A typical temperature cycle is shown in Figure 6.

During E-beam evaporation, the thickness of the Ti film is monitored by a quartz crystal oscillator. After diffusion, waveguide ridges about 2.5 times as high as the original Ti thickness are present. These ridges are used as registration marks in later photolithographic processing.

Typically, we have found that the parameters shown in Table 2 will generate single-mode guides in z-cut LiNbO<sub>3</sub> for the TE polarization.

#### 4. Coupling Length Between Waveguides

Since there is no analytical description for the modal field of a single diffused channel waveguide, no closed-form expression for the coupling length  $\ell$  is available for directional couplers. However, the coupling between two uniform index channel waveguides has been analyzed.<sup>5</sup> In this case,

$$\ell = \ell_0 \exp\left(\frac{d}{\gamma}\right)$$



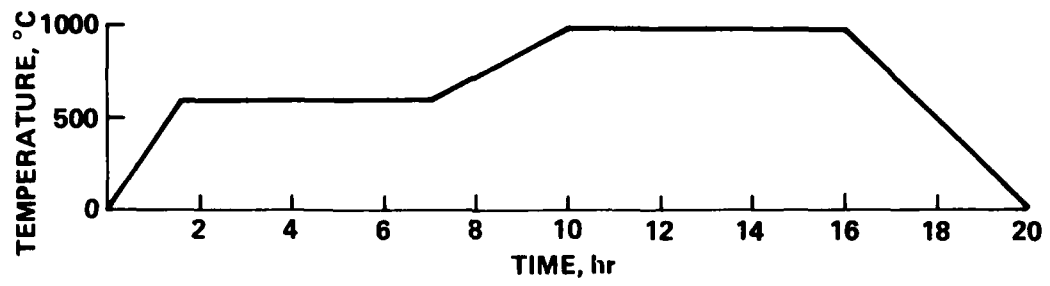


Figure 6. Diffusion temperature cycle for waveguide formation.

where  $\ell_0$  depends on waveguide parameter but is independent of  $d$ , the separation between guides. The quantity  $\gamma$  is the evanescent penetration depth. Qualitatively,  $\ell_0$  depends on the shape of the fields within each guide. For the uniform refractive index channel guides, we can write

$$\ell_0 = \frac{\pi k_x \sqrt{1 + k_x^2 \gamma^2}}{4 k_z^2 \gamma}$$

where  $k_x$  is the component of the propagation constant along the direction of separation of the guides, and  $k_z$  is the component along the length of the guides. We have used this theory to predict the general behavior we would expect to see experimentally. Figure 7 shows some of these results.

Table 2. Single-Mode Diffusion Parameters

$\lambda$	Guide Width, $\mu\text{m}$	Ti Thickness, $\text{\AA}$	Diffusion Temperature, $^{\circ}\text{C}$	Diffusion Time, hr
0.6328	3	200-350	1000	6
0.82	3	400-500	1000	6
0.82	4	350-450	1000	6
1.06	5	470-500	1000	6

7128

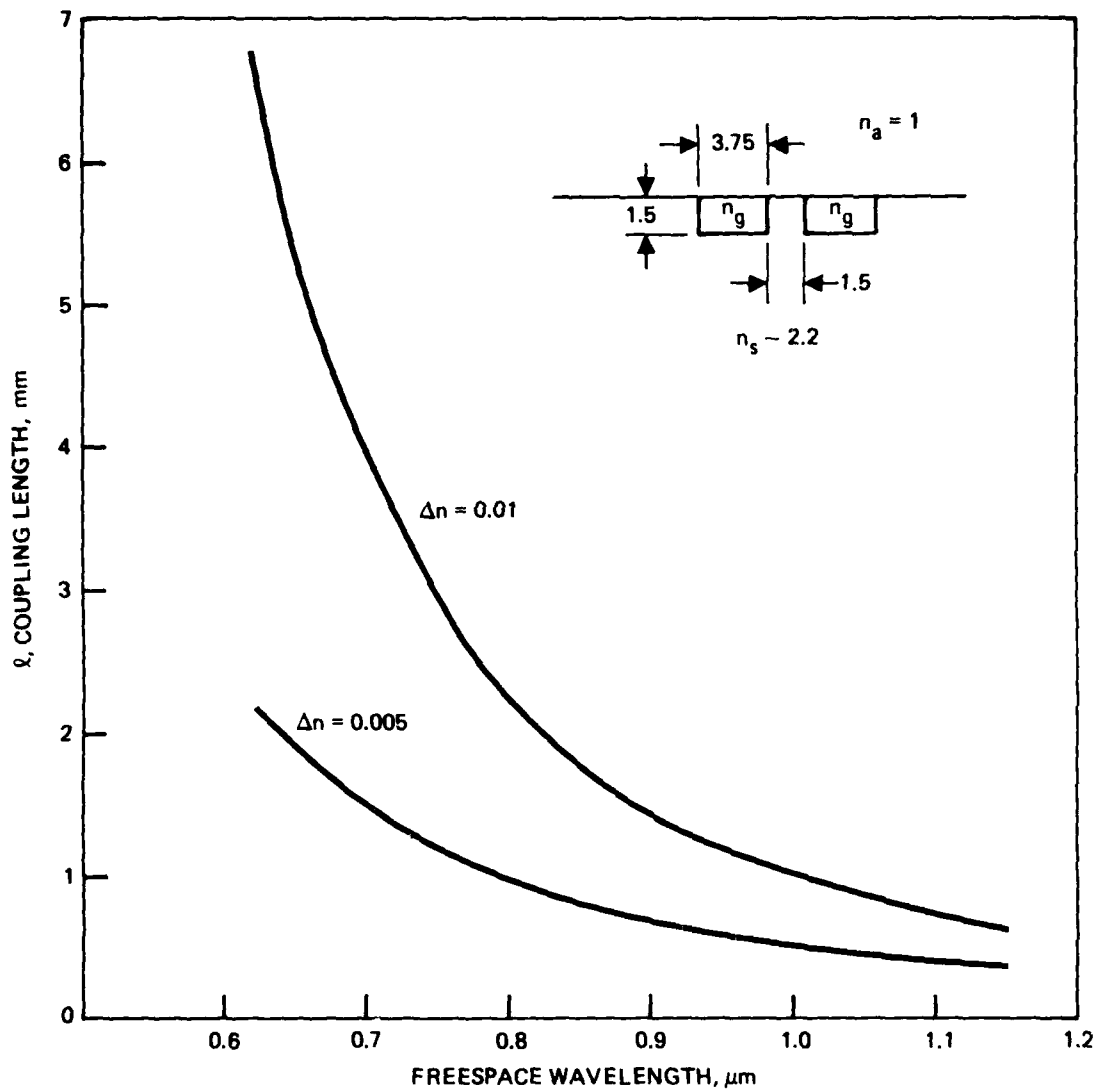


Figure 7. Coupling length versus wavelength for uniform rectangular guides. The index of the superstrate is 1. The substrate has an index of 2.2. The guide index is  $2.2 + \Delta n$ . The guide dimensions are shown in the insert.

Recent articles by Schmidt et al.<sup>6</sup> have contained experimental data for the coupling length for various guide configurations and wavelengths. These data are shown in Figure 8. For  $d = 3 \mu\text{m}$ , the following Ti thicknesses and waveguide widths produce an  $\ell \sim 2 \text{ mm}$ :

$\lambda, \mu\text{m}$	Ti Thickness, $\text{\AA}$	W, $\mu\text{m}$
0.6328	300	3
0.83	400	4
1.06	460	5

The method for determining the coupling coefficient is illustrated in Figure 9. The output intensity from the two channels assuming only one has been excited is proportional to  $\sin^2(\kappa L + \phi)$  and  $\cos^2(\kappa L + \phi)$  where  $\kappa$  is the coupling coefficient,  $L$  is the interaction length and  $\phi$  is the amount of coupling that has taken place in the transition to and from the interaction region. Thus,

$$\kappa L + \phi = \tan^{-1}(\sqrt{\text{Ratio}})$$

where ratio = the ratio of the two output intensities. The data obtained for a sample with  $570\text{\AA}$  of Ti,  $5 \mu\text{m}$  wide guides,  $3 \mu\text{m}$  gap and varying interaction lengths and a  $1.15 \mu\text{m}$  HeNe laser are plotted in Figure 10. The coupling length ( $\nu = \pi/2$ ) from these plots are  $\ell = 3.5 \text{ mm}$  and  $\ell = 1.9 \text{ mm}$  for the TM and TE modes respectively.

The experiments to optimize the fiber-to-waveguide coupling at a wavelength of  $.83 \mu\text{m}$  identified  $470 \text{\AA}$  of Ti-diffused for 8 hours as parameter which gives coupling approaching theoretical limits. With waveguides formed using these parameters the experimentally determined coupling length with a  $3 \mu\text{m}$  gap is  $2.3 \text{ mm}$ .

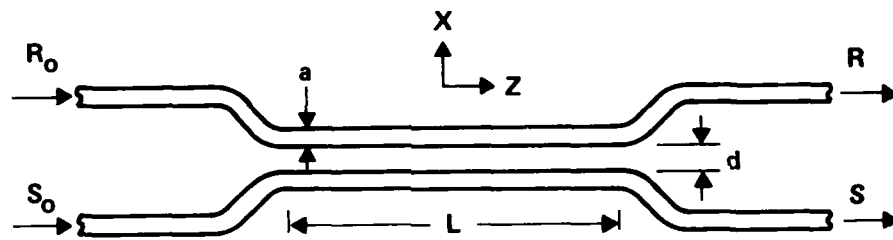


Figure 8(a). Top view of a waveguide directional coupler where  $L$  is the coupler length,  $a$  is the waveguide width, and  $d$  is the separation between the waveguides in the interaction region.

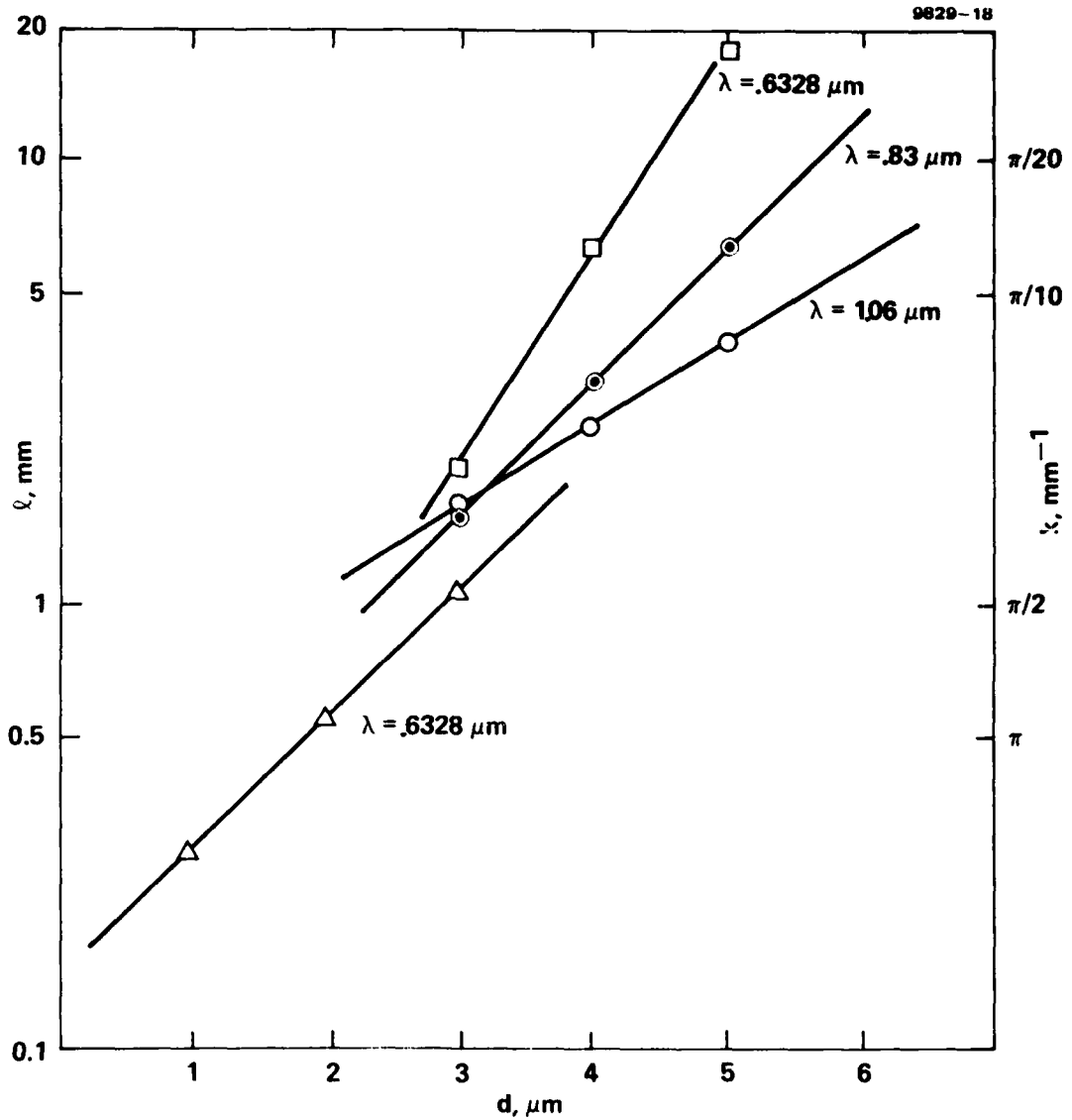
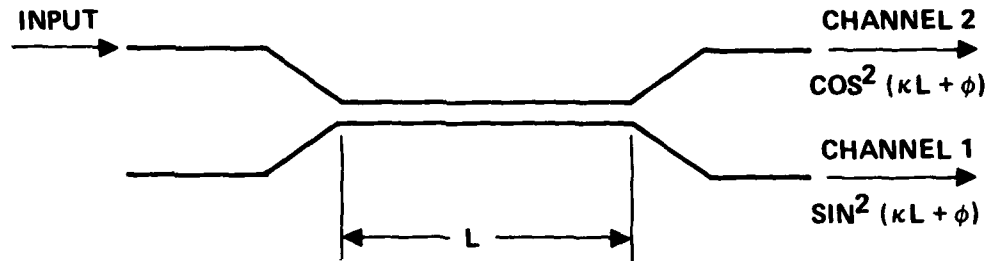


Figure 8(b). Coupling coefficient: Ti-diffused  $\text{LiNbO}_3$  waveguides at 1.06-, 0.83-, and 0.6328- $\mu\text{m}$  wavelengths as a function of waveguide separation. For each wavelength, the waveguides were fabricated so as to be single mode using the following fabrication parameters: ( $\square$ )  $\lambda = 0.6328 \mu\text{m}$ ,  $\tau$  (Ti metal thickness) = 300  $\text{\AA}$ ,  $a = 3 \mu\text{m}$ ; ( $\Delta$ )  $\lambda = 0.6328 \mu\text{m}$ ,  $\tau = 300 \text{\AA}$ ,  $a = 2 \mu\text{m}$ ; ( $\odot$ )  $\lambda = 0.83 \mu\text{m}$ ,  $\tau = 400 \text{\AA}$ ,  $a = 4 \mu\text{m}$ ; and ( $\circ$ )  $\lambda = 1.06 \mu\text{m}$ ,  $\tau = 460 \text{\AA}$ ,  $a = 5 \mu\text{m}$ .



$\kappa$  = COUPLING COEFFICIENT

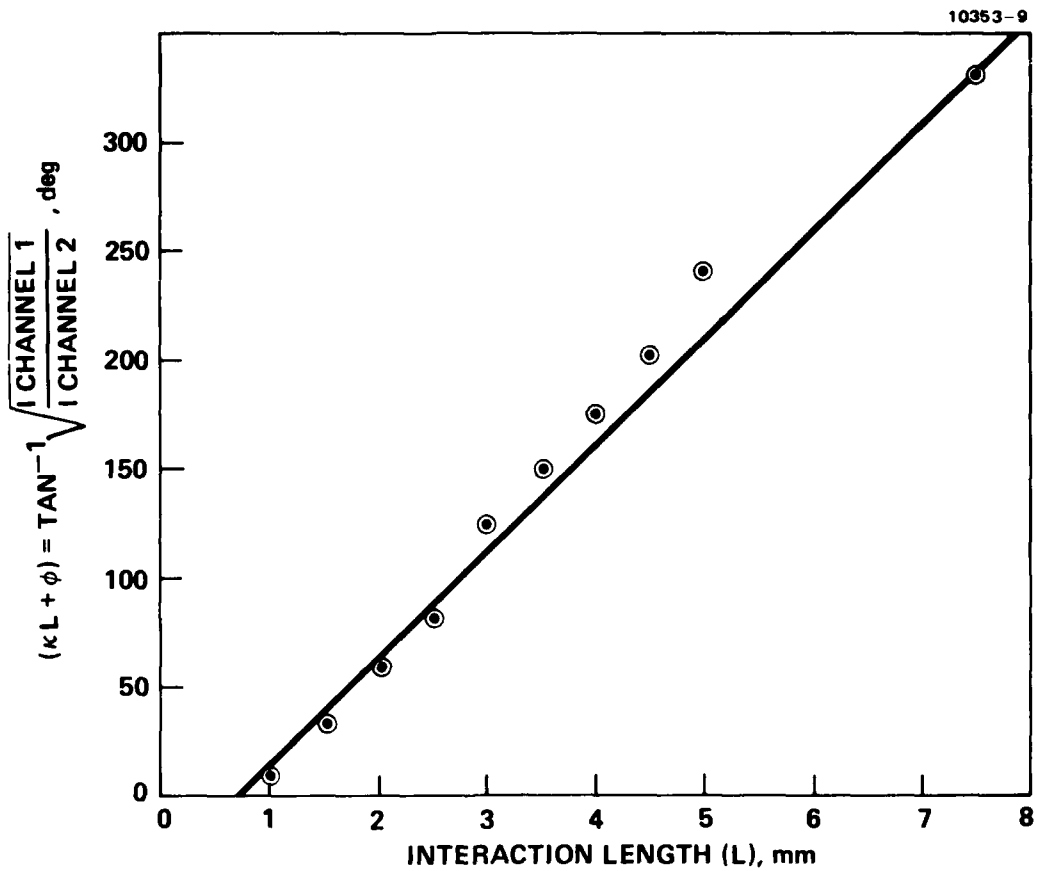
$L$  = INTERACTION LENGTH

$\phi$  = TOTAL COUPLING IN TRANSISTIONS REGIONS

$$\kappa L + \phi = \text{TAN}^{-1} \left( \frac{I \text{ CHANNEL 1}}{I \text{ CHANNEL 2}} \right)^{1/2}$$

ON MASK  $L = 1, 1.5, 2, 2.5, 3, 3.5, 4, 4.5$  AND  $7.5$  mm

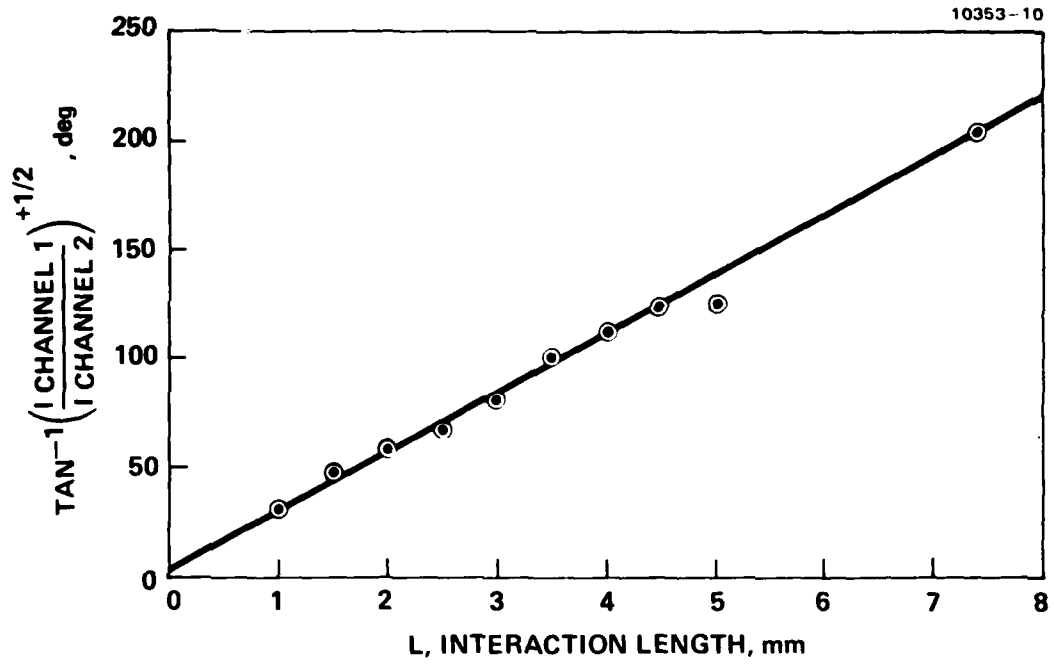
Figure 9. Method for determining the coupling coefficient,  $K$ .



(a) TE mode

Figure 10. Experimental data determining the coupling coefficient at a  $1.15 \mu\text{m}$  wavelength for waveguides  $5 \mu\text{m}$  wide and  $3 \mu\text{m}$  gap. The waveguides were formed from  $570 \text{ \AA}$  of Ti diffused for 6 hrs at  $1000^\circ\text{C}$ .





(b) TM mode.

Figure 10. Continued.

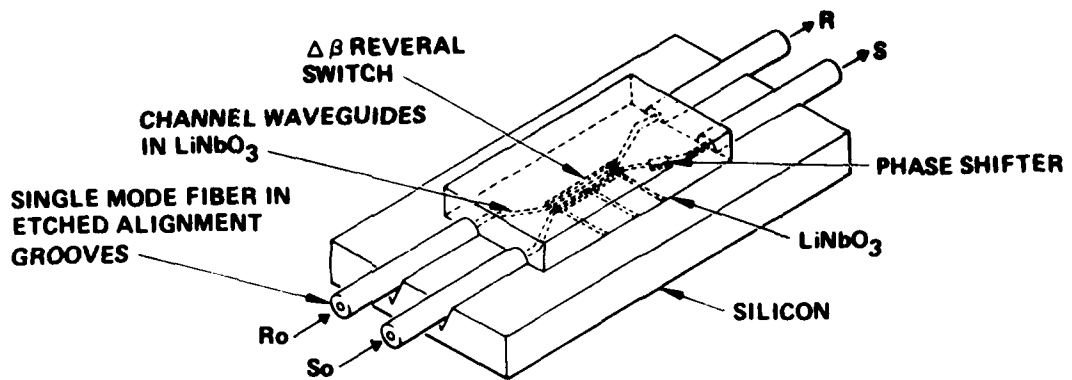
## B. FIBER ATTACHMENT

### 1. Coupling Apparatus

We had proposed to use the fiber attachment technique illustrated in Figure 11. To hold the ITT single-mode fibers, V-grooves were to be etched in  $\langle 100 \rangle$ -oriented Si wafers with KOH. With this technique, the groove widths are such that the fiber core is just above the Si surface, and the photolithographic masks have matching groove and guide center-to-center spacings. But we found that, when the  $\text{LiNbO}_3$  chip is flipped and placed on the Si surface, the fibers and channel guides cannot be easily aligned. This is particularly true of the output pair of fibers. This is primarily because both sides must be realigned on small rotations of the chip and because the visual alignments available were not adequate to position the guides exactly in the center of the V grooves. These difficulties forced us to develop a new technique for fiber attachment.

This new technique is illustrated in Figure 12, with a photograph of the deliverable. The V-groove technology is again used to establish the fiber-to-fiber separation, but a separate Si chip is used on each face of the  $\text{LiNbO}_3$  sample. After the fibers are positioned in the grooves, the Si and fibers are polished such that the fiber and Si edge are aligned (see Figure 13). The first two (input) fibers can then be aligned and fixed into place before the second is aligned. In addition, the sample face is not flipped down on the Si surface, thus making electrical connection easier. The fixing is done with the epoxy.

The fixture is designed such that the Si chips can be adjusted into place with external micropositioners, epoxied into place, and have the positioner removed. With the early fixtures it was found that the above process does not leave everything in an optimum position; therefore, we have designed into this later fixture the ability to adjust each Si chip independently by several microns in the plane and normal to the plane of the  $\text{LiNbO}_3$  sample. The minimum throughput loss was 7.8 dB; a value  $\sim 2$  dB larger than theoretically predicted.



SWITCH

- CHARACTERISTIC PARAMETERS
- INTERACTION LENGTH,  $L$
- COUPLING COEFFICIENT,  $\kappa$
- CONVERSION LENGTH,  $l = \pi/2\kappa$
- PROPAGATION CONSTANT MISMATCH  $\Delta\beta = \beta_1 - \beta_2$

• STATE DEFINITIONS

- ⊗  $R_0 = 1, S_0 = 0; R = 0, S = 1$
- ⊙  $R_0 = 1, S_0 = 0; R = 1, S = 0$

PHASE SHIFTER

- $\Delta n = \frac{1}{2} n^3 r_{13} E_3$
- $\Delta\phi = \frac{2\pi}{\lambda_0} \Delta n D$

Figure 11. Schematic of the four-port optical switch module.

10353 13

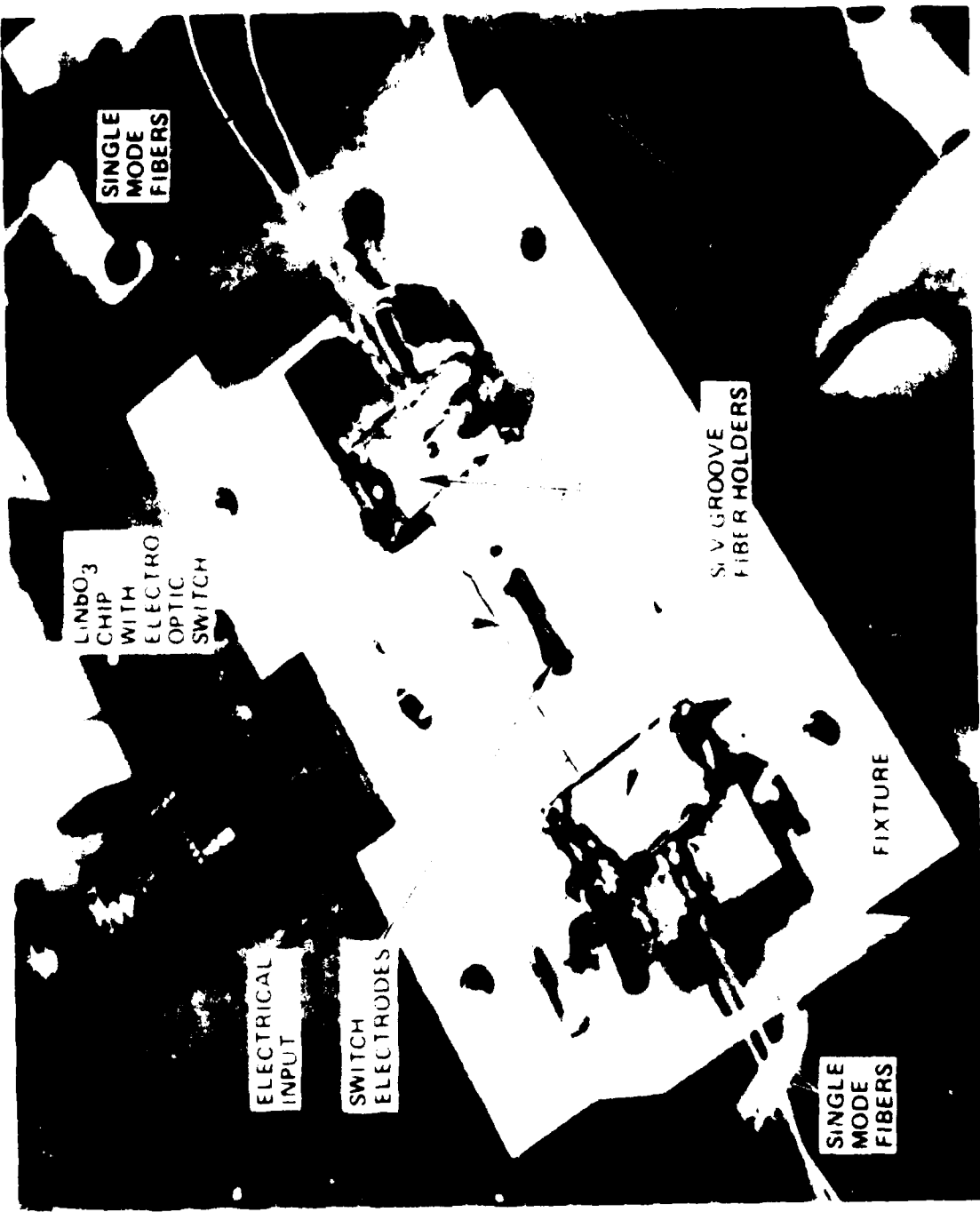
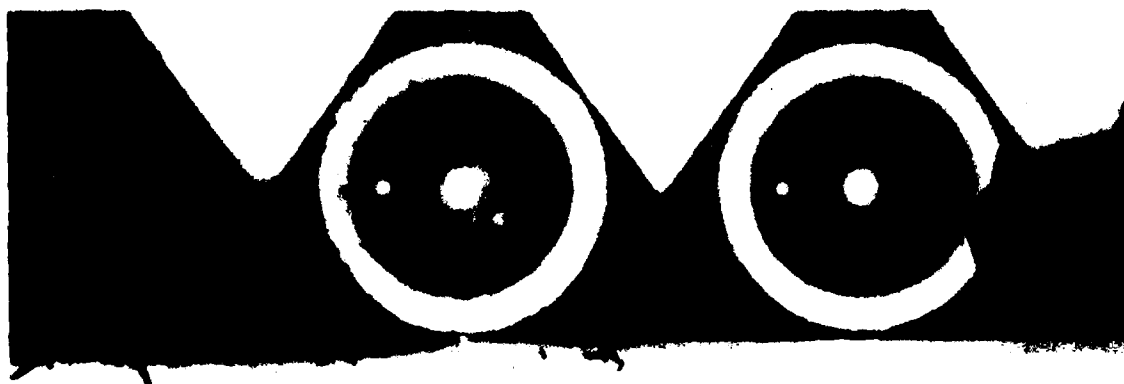


Figure 12. Photograph of deliverable illustrating single mode fibers and switch.

M10184-5



10 20 30 40 50  
microns

Figure 13. Photograph of the polished end of Si wafer with V grooves containing single mode fibers.

## 2. Fiber-to-Channel Coupling Performance

The theoretical coupling between a fiber and channel waveguide has been described by Hocker and Burns.<sup>7</sup> Their approach is to describe the mode of the channel waveguide by a rectangular Gaussian beam with waists in beam half widths of  $W_x$  and  $W_y$ . The  $HE_{11}$  mode of the fiber can be approximated by a circular Gaussian with waist  $a$ . Cohen<sup>8</sup> has shown that the coupling coefficient between rectangular and circular Gaussians is an optimum at the waist of the two beams and is given by

$$K = \frac{4}{\left(\frac{W_x}{a} + \frac{a}{W_x}\right) \left(\frac{W_y}{a} + \frac{a}{W_y}\right)}$$

The total coupling from fiber to channel is then given by

$$K' = T I_x^2 I_y^2 I_2^4 K$$

where  $T$  is the transmissivity,  $I_x$  is the overlap of channel mode in the  $x$  direction and a Gaussian of waist  $W_x$ ,  $I_y$  is the overlap of channel mode in the  $y$  direction and a Gaussian of waist  $W_y$ , and  $I_2$  is the overlap of the  $HE_{11}$  mode of the fiber and a circular Gaussian of waist  $a$ . The value of  $I_x$ ,  $I_y$ , and  $I_2$  were shown to be on the order of 0.98.

For long diffusion times as compared with the time required to diffuse all the source material from the surface into the bulk, the index profile for a strip of infinite extent in the  $z$  direction and extending from  $x = -W/2$  to  $x = W/2$  in the  $x$  direction is (the substrate occupies the space  $y = 0$ )

$$n^2(x,y) = n_b^2 + (n_s^2 - n_b^2) f(y/D) g(2x/W)$$

$$f(y/D) = \exp(-y^2/D^2)$$

$$g(2x/W) = \frac{1}{2} \left\{ \operatorname{erf} \left[ \frac{W}{2D} (1 + 2x/W) \right] + \operatorname{erf} \left[ \frac{W}{2D} (1 - 2x/W) \right] \right\} .$$

Because of lateral diffusion, the geometrical aspect ratio of the guide is not  $W/D$ , but is defined as  $2x_{1/2}/D$ , where

$$g\left(\frac{2x_{1/2}}{W}\right) = \frac{1}{2} g(0) .$$

The geometrical aspect ratio is plotted in Figure 14 versus the quantity  $W/D$ . For a given  $W$  and increasing  $D$  (increased diffusion time or temperature), the geometrical aspect ratio decreases to  $\approx 1.7$  for  $W = D$  and remains constant at this value. According to the calculations of Hocker and Burns, this corresponds to the maximum coupling, although, as can be seen from Figure 15(b), the decrease with increasing  $2x_{1/2}/D$  is slow. These calculations are based on the solid curve in Figure 15(a), which is a fit to calculated data for typical diffusion profiles and effective index of the guides determinable from  $b_0$ . The data show that approximately 80% coupling may be achieved if all parameters are optimized in a single diffusion; this corresponds to 64% throughput from fiber to fiber if the propagation and bend losses are neglected (64% corresponds to  $\approx 2$  dB loss).

A simple computer program has been written to determine the angular and displacement tolerances that must be maintained. This program simply calculates the overlap integral between two Gaussian beams as a function of angle and displacement. Some of the data from this program is shown in Figure 16. It is interesting to compare this data to the experimental data of Noda et al.<sup>9</sup> shown in Figure 17. Basically,

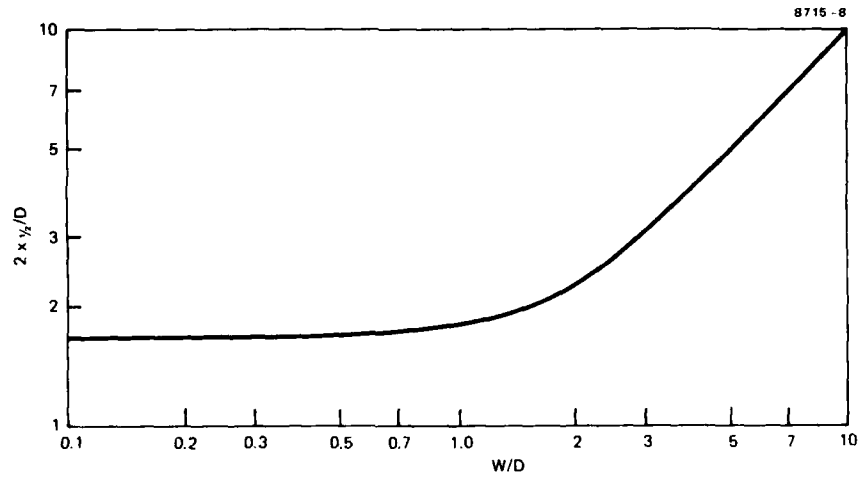


Figure 14. The geometric aspect ratio of an isotropically diffused channel waveguide plotted versus the ratio of the undiffused channel width  $W$  to the diffusion length  $D$ .



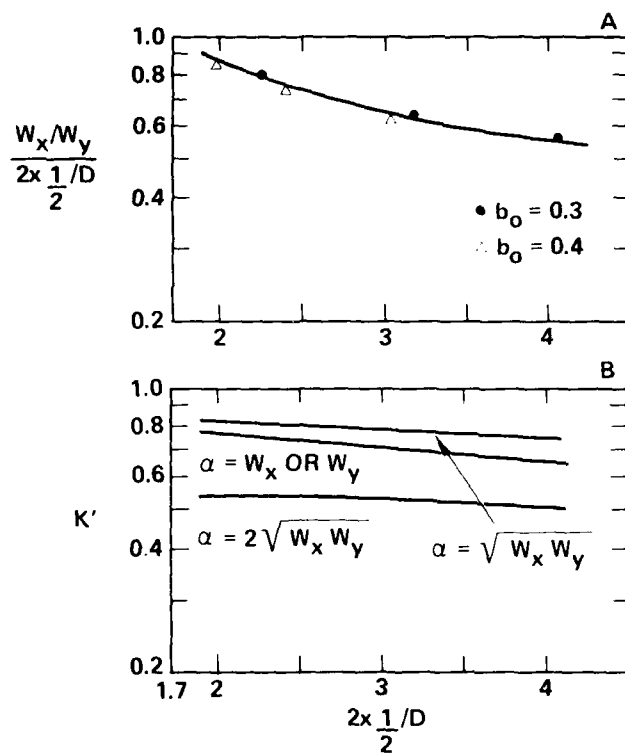
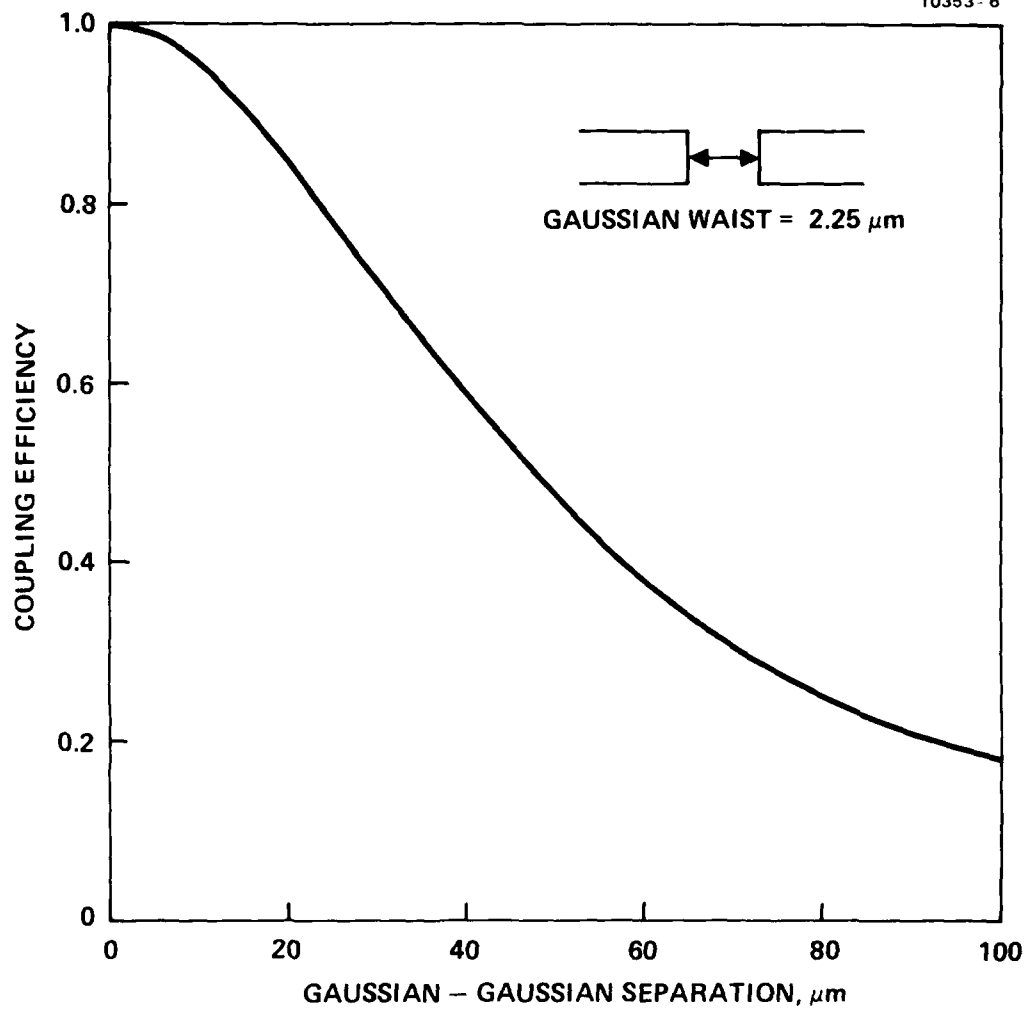
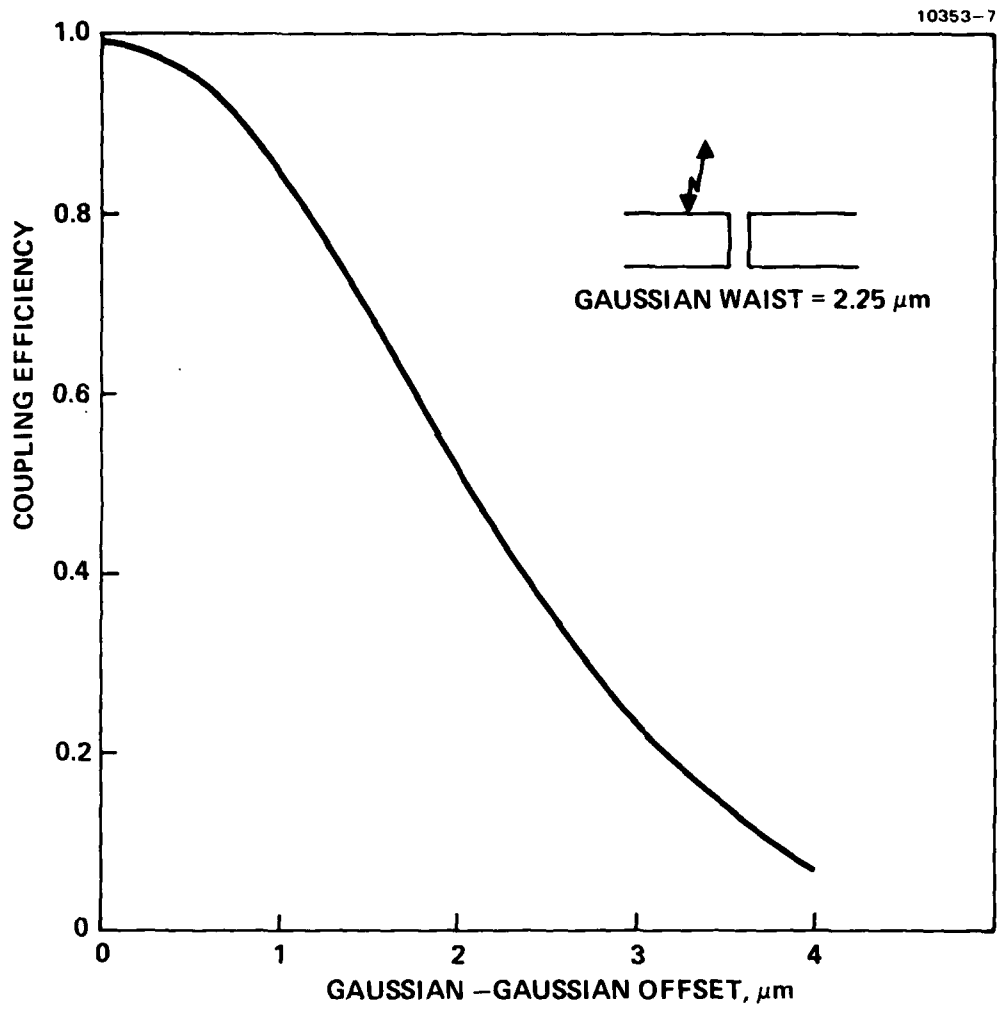


Figure 15.  
 Plotted in (a) is the ratio of the modal aspect ratios to the geometric aspect ratio for the first-order mode in several diffused channel waveguides. In (b) is the power coupling coefficient for end fire coupling between a circular fiber with mode radius  $\alpha$  and a diffused channel waveguide with mode half widths  $W_x$  and  $W_y$ . Both quantities are plotted versus the geometric aspect ratio of the diffused channel waveguide. After Hocker and Burns.



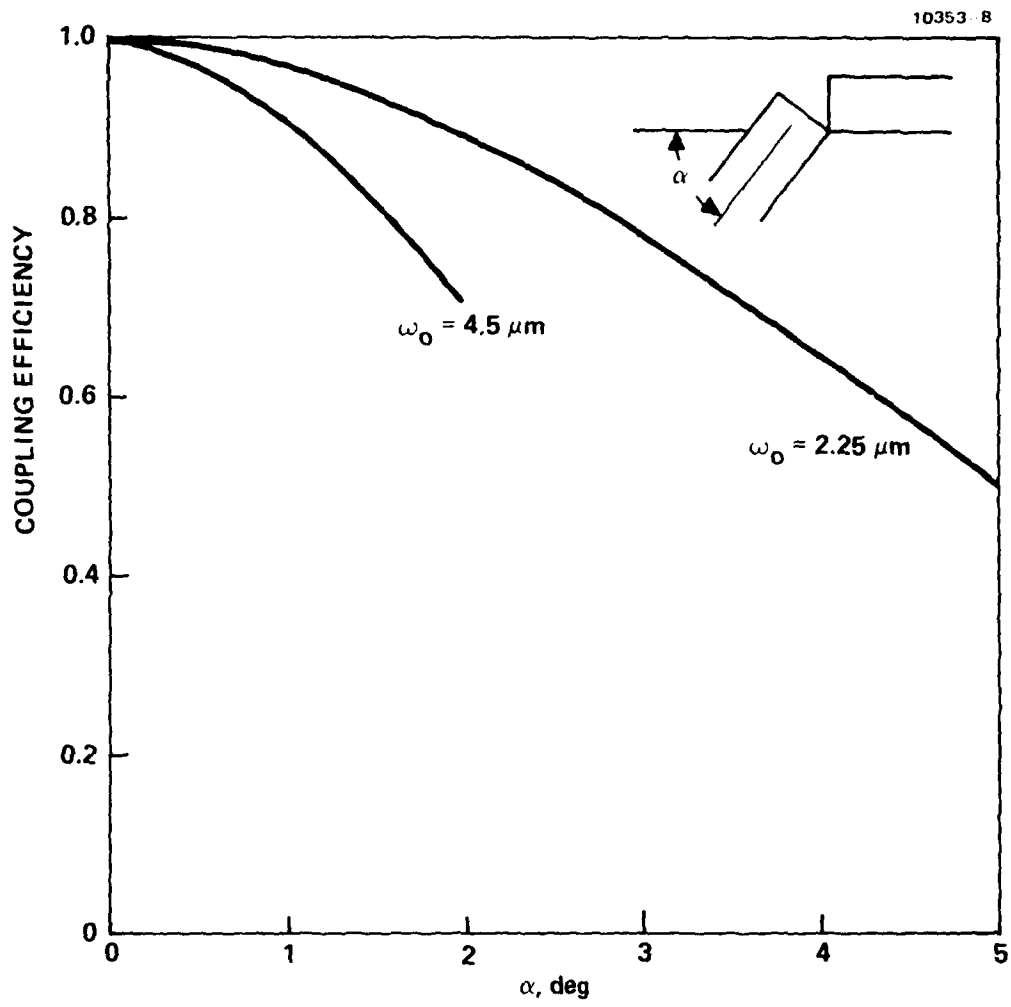
(a) Separation along Z direction

Figure 16. Coupling coefficients associated with Gaussian beams.



(b) Separation along direction perpendicular to Z axis

Figure 16. Continued.



(c) Angular misalignment

Figure 16. Continued.

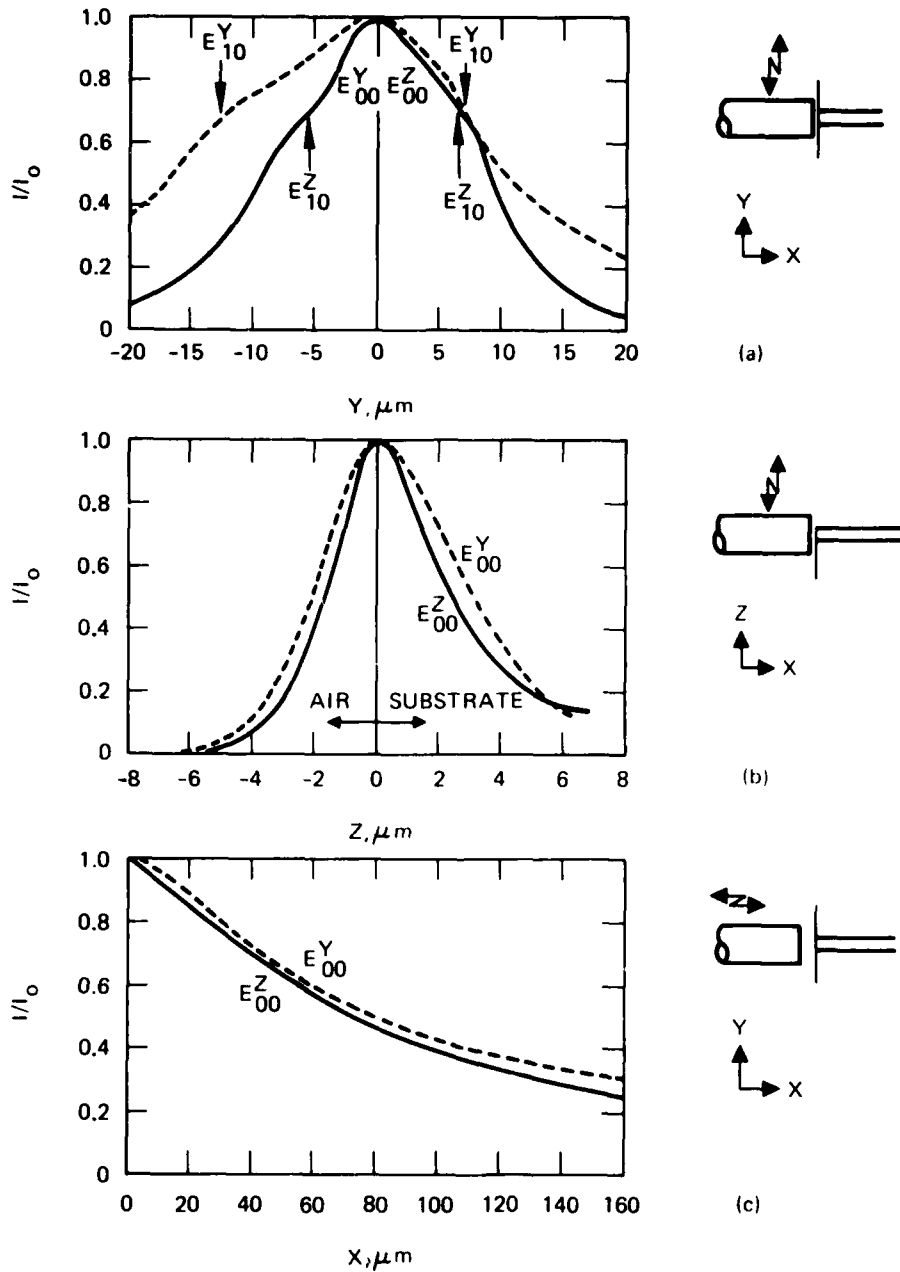


Figure 17(a). Variation in insertion ratios versus axial displacement (a) along the y direction, (b) along the z direction, and (c) along the x direction. (After Noda et al.<sup>4</sup>)

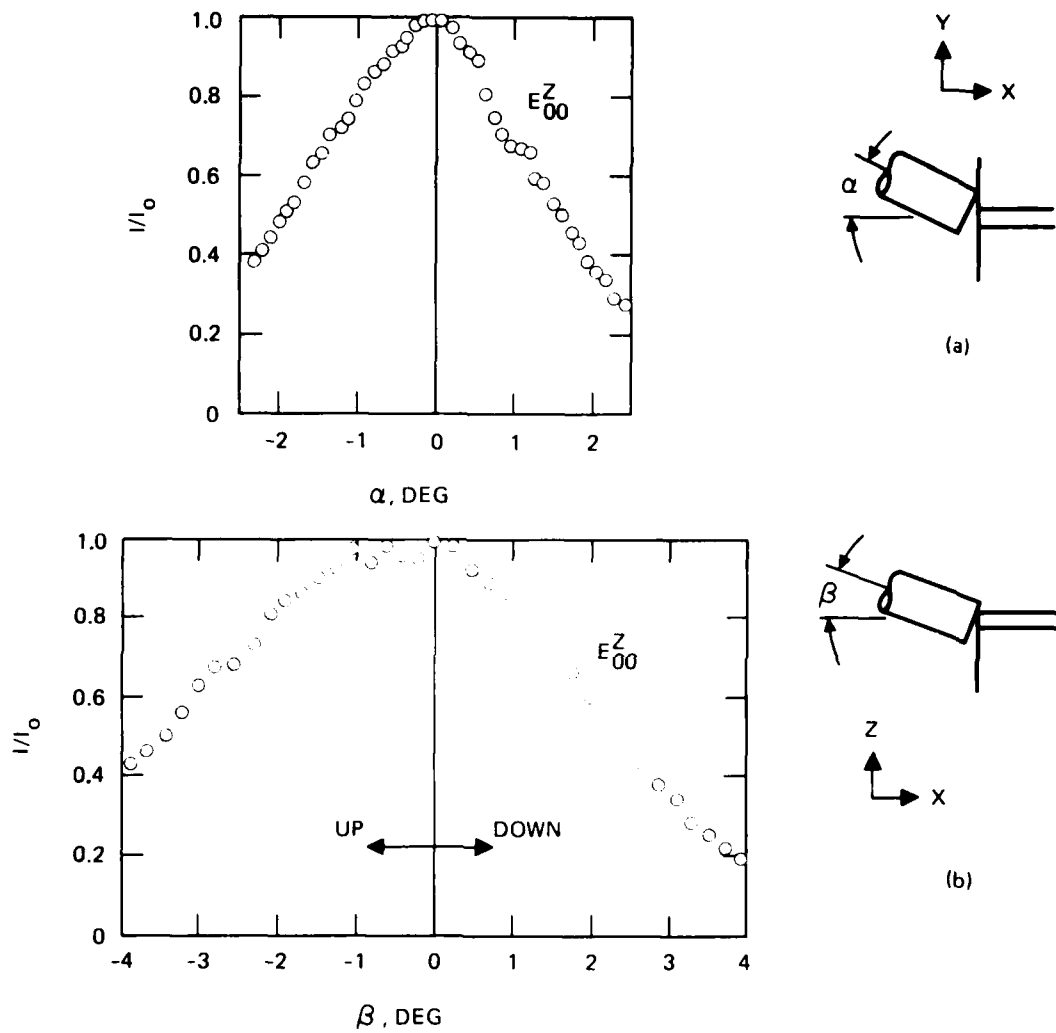


Figure 17(b). Variation in insertion ratios versus angular misalignments (a) horizontally and (b) vertically.

the calculations reinforce Noda's experimental data except for the angular tolerance. The decreased waist associated with the smaller fiber core diameter increases the tolerance limits.

b. Experimental Coupling Measurements

In order to optimize the single mode fiber to integrated optic channel waveguide coupling waveguide samples with different waveguide widths, Ti depths and diffusion times were fabricated. In these experiments, an ITT single mode fiber with a 4.5  $\mu\text{m}$  core coupled to a laser diode with a wavelength of 0.83  $\mu\text{m}$  were used. The waveguide samples contained straight waveguides; the following fabrication parameters were used:

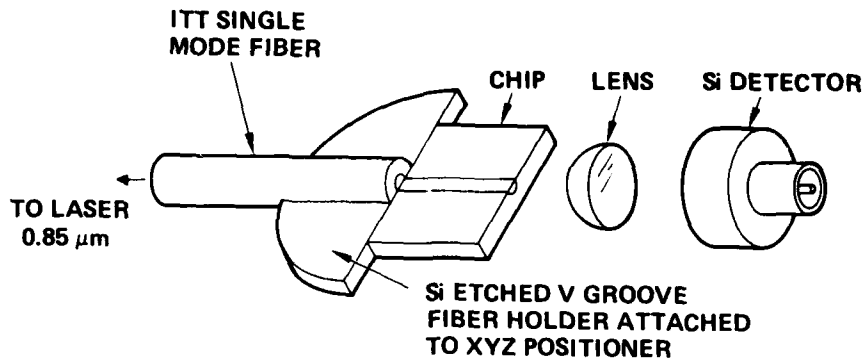
- Ti thickness as of 430  $\text{\AA}$  and 470  $\text{\AA}$
- Diffusion times of 4, 6 and 8 hrs, and
- Waveguide width from 1  $\mu\text{m}$  to 10  $\mu\text{m}$  in 1/2  $\mu\text{m}$  steps.

With these samples we have achieved theoretically predicted values for the coupling coefficient.

The experimental setup illustrated in Figure 18 has been used in the evaluation. The detected light has been corrected by the following values to obtain the coupling coefficient:

- lens loss of 1.1 dB (measured value)
- propagation loss of 1 dB (assumed may be lower)
- reflection loss of 0.5 dB (theoretical value).

The values obtained for the TE polarization versus waveguide width are plotted in Figure 19; values have been plotted only for single mode guides. The 430  $\text{\AA}$  samples had excellent waveguides for all three diffusion times. The 470  $\text{\AA}$  samples appeared incompletely diffused for the 4 and 6 hr diffusions. The 8-hr diffusion samples produced excellent waveguides.



COUPLING LOSS = TOTAL THROUGHPUT LOSS MINUS  
1.1 dB LENS LOSS  
1.0 dB PROPAGATION LOSS  
0.5 dB REFLECTION LOSS

Figure 18. Schematic of the fiber-to-chip coupling loss measurement technique.

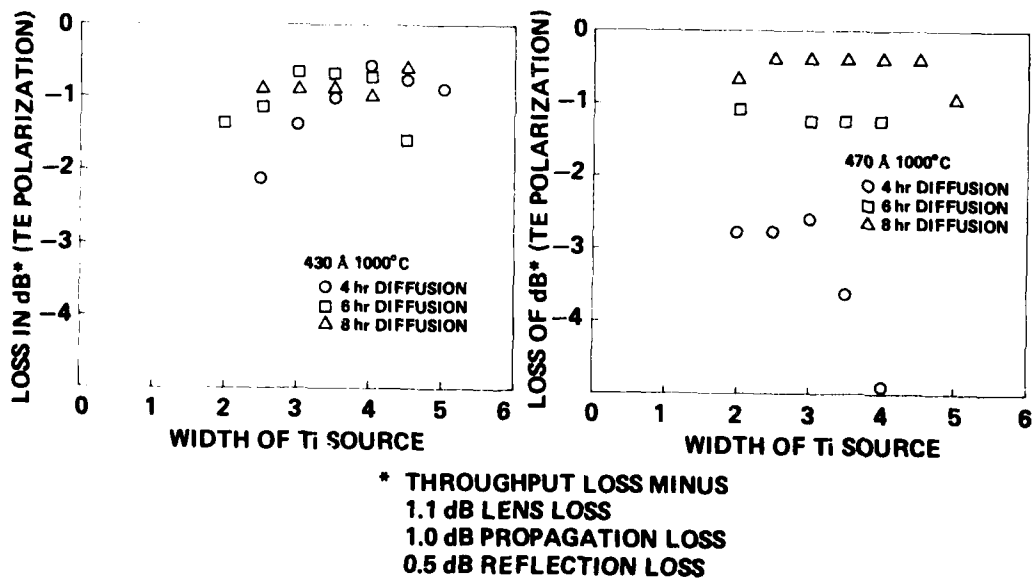


Figure 19. Coupling loss between ITT single mode fibers and Ti diffused strip waveguides of different widths for different diffusion times and Ti depths.



At the 5  $\mu\text{m}$  waveguide width the 430  $\text{\AA}$  sample gave a coupling loss below 0.7 dB. The 470  $\text{\AA}$  8-hr diffusion sample gave the lowest coupling coefficient of 0.4 dB for a wide range of waveguide widths. These values must be viewed as lower bounds since they are corrected measurements based on an assumed propagation loss; however, we can be assured of a coupling loss of less than 1 dB.

Figure 20 shows the polished edge of a  $\text{LiNbO}_3$  chip illuminated from above. The waveguides are clearly visible; a cross section ratio of  $\approx 2:1$  exists. These waveguides were formed with 470  $\text{\AA}$  of Ti and a 1000°C, 8-hr diffusion. The width of the Ti was 4  $\mu\text{m}$ . This serves as an experimental confirmation of the Hocker and Burns theory that optimum coupling occurs for a W/D of 2 or below.

### C. WAVEGUIDE LOSSES

In addition to simple propagation loss ( $\approx 1$  dB/cm), there are other sources of loss associated with an optical circuit that do not exist in straight waveguides. The two primary sources are:

- Waveguide bends and displacement.
- Metal electrode placement on waveguides.

Research that has been done in these areas at HRL are discussed below.

In the switch waveguide mask there typically are two additional sources of loss that do not exist with straight waveguides. A schematic of one of our waveguide masks is shown in Figure 21; note that the mask is not drawn to scale. These are the bends and waveguide displacement at the connection between angled and non-angled sections. We have analyzed what the expected loss should be for a bend and a displacement between straight guides. The initial calculations were done using the mode profiles obtained by the Marcatili<sup>5</sup> dielectric waveguide analysis. The second analysis was done using Gaussian profiles; it gives simple formulas that are dependent on the Gaussian waist,  $w$ , and match the other

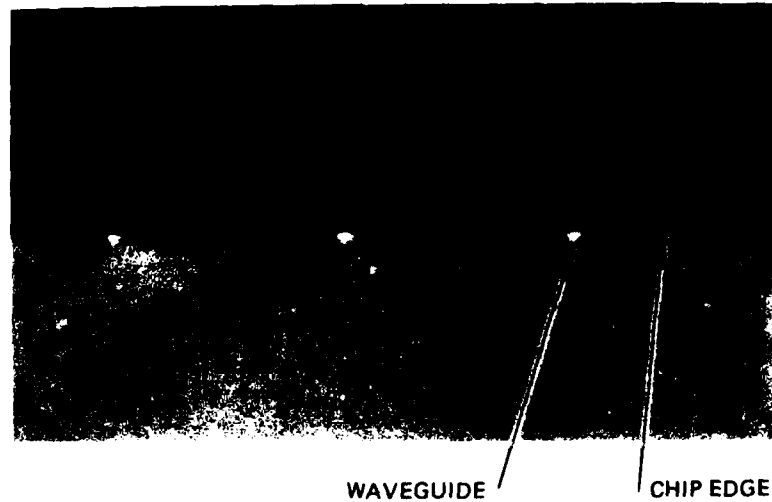


Figure 20. Photograph of a polished edge of an  $\text{LiNbO}_3$  chip with Ti-diffused waveguides.

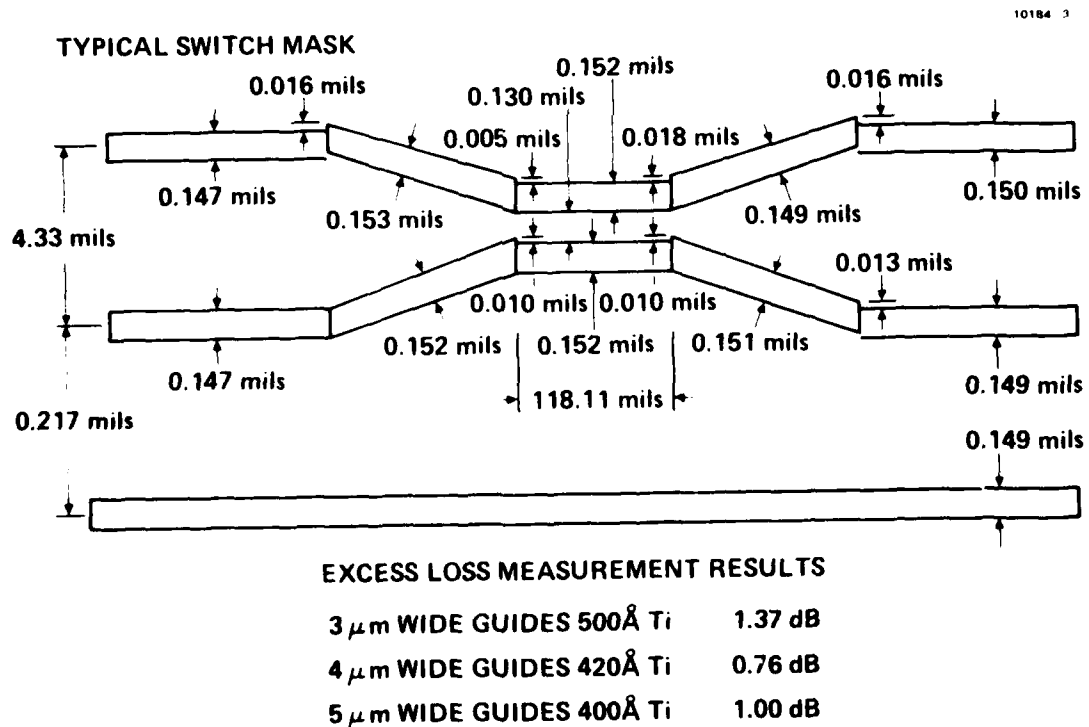


Figure 21. Sources of additional losses in integrated optics circuits related to mask making accuracy. Note that the waveguide configuration is not drawn to scale. The horizontal extent is approximately 0.6 in. this is due to the  $0.5^\circ$  bends.

calculation if the appropriate waist is chosen. A more complete discussion of these analyses are given in the Appendix. For the bend shown in Figure 22, the transmission is given by

$$t = e^{-k^2 a^2 \sin^2 \theta / 4}$$

where  $k$  is the propagation constant and  $\theta$  is the bend angle in the waveguide. For the displacement shown in Figure 23, the transmission is given by

$$t = e^{-\Delta^2 / \lambda^2}$$

where  $\Delta$  is the displacement between waveguides. These results are plotted in Figures 22 and 24 for 4 and 5  $\mu\text{m}$  waveguides. On our 4  $\mu\text{m}$  mask, which has four  $0.5^\circ$  bends and approximately 0.4  $\mu\text{m}$  displacement at the waveguide interconnections, the expected additional loss is 0.1 dB, which corresponds with the experimental results below.

Three samples with straight guides and switch patterns showing excellent transmission have been measured. These three samples were diffused for 6 hrs and have

- a. 3  $\mu\text{m}$  wide Ti sources 500  $\text{\AA}$  thick
- b. 4  $\mu\text{m}$  wide Ti sources 420  $\text{\AA}$  thick
- c. 5  $\mu\text{m}$  wide Ti sources 400  $\text{\AA}$  thick.

The throughput for the switch patterns is consistently lower than the straight guides. The excess losses caused by the bends in the samples were 1.37, 0.76 dB, and 1 dB for samples a, b, and c, respectively.

The second source of additional loss associated with an optical circuit is the placement of electrodes on the chip such that the metal interferes with the light. The electrodes placed directly on the  $\text{LiNbO}_3$  waveguides as required for the Z-cut  $\text{LiNbO}_3$  switch are a source of

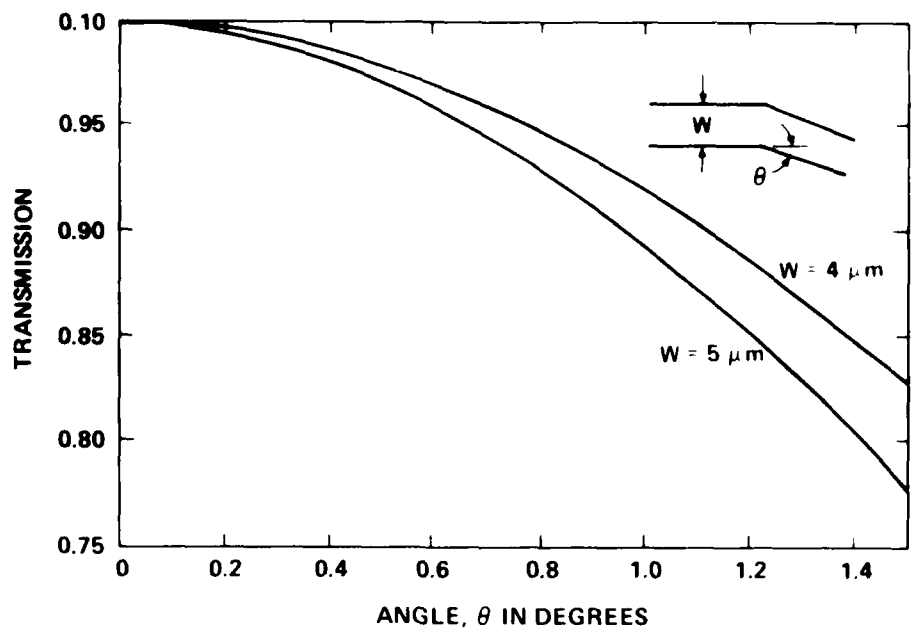


Figure 22. Calculated transmission through a waveguide bend formed by the intersection of two straight waveguides.

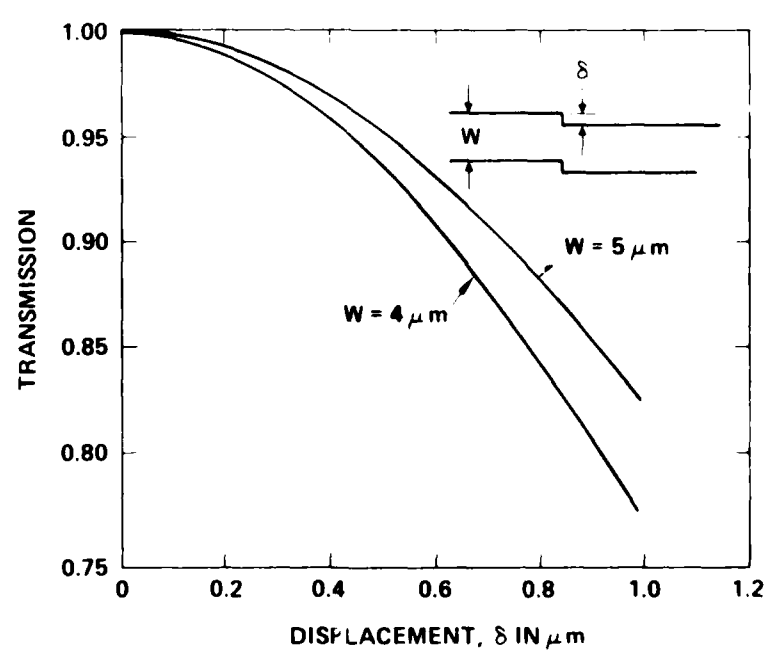
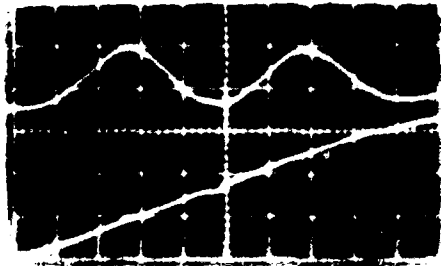


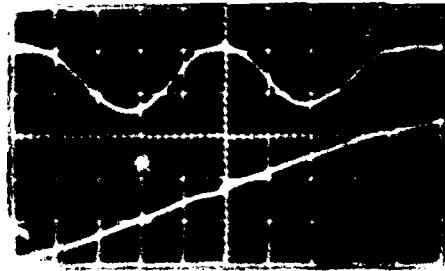
Figure 23. Calculated transmission through a waveguide discontinuity formed by a slight lateral displacement.

TE MODE OPERATION

1ST OUTPUT PORT



2ND OUTPUT PORT



DRIVE SIGNAL LOWER TRACE 50 VOLTS/DIV

Figure 10. TE mode operation.

TM OPERATION



ZERO OPTICAL INTENSITY

DRIVE SIGNAL LOWER TRACE 50 VOLTS/DIV

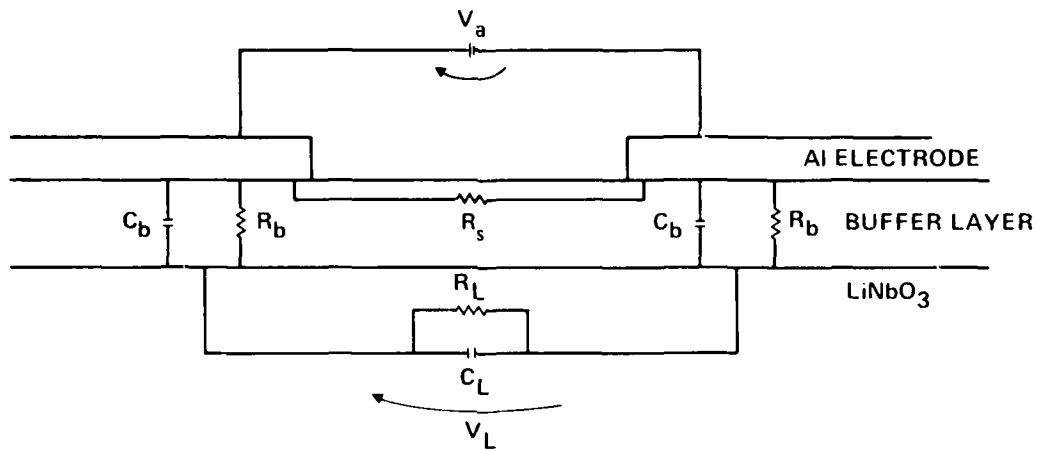
Figure 11. TM mode operation.

Figure 12. Waveform from a reversal switch operation at 60 Hertz.

propagation loss (1 dB/mm for the TE mode and 10 dB/mm for the TM mode). Therefore, it is desirable (and in fact necessary for low-loss chips) to isolate the electrodes from the  $\text{LiNbO}_3$  surface with a low-loss dielectric if the Z-cut configuration is to be used. This isolation reduces the propagation losses for both polarizations, making it possible to switch the TM polarization with the larger  $r_{33}$  electrooptic coefficient. Figures 24 a and b presents switching curves displayed on an oscilloscope at 60 Hertz. The switching voltage for the TM mode is approximately 1/3 that of the TE mode corresponding to the ratio  $r_{33}/r_{13}$ .

The presence of a buffer layer has important ramifications on low-frequency operation. This follows because the buffer layers and the  $\text{LiNbO}_3$  typically have different resistivities. This can be shown with a simple equivalent circuit model Figure 25. The model shows three capacitors with corresponding leakage resistors. The three capacitors complete the electrical circuit between the electrodes. Two capacitors are across the buffer layer and one across the  $\text{LiNbO}_3$ . This is equivalent to having three dielectrics with different leakage resistances between the plates of a parallel plate capacitor. At dc operation, the voltage across the three capacitors or dielectrics is a simple voltage division of the leakage resistance. If the resistance across the  $\text{LiNbO}_3$  is much less than the resistance of the two buffer layer regions in dc steady-state, there will be only a small voltage or corresponding electric field across the  $\text{LiNbO}_3$ . Conversely, if the resistance associated with the buffer layers is small compared with that associated with the  $\text{LiNbO}_3$ , the electric field and associated voltage will be largest in the  $\text{LiNbO}_3$ .

For the .95  $\mu\text{m}$  wavelength we have fabricated and tested 4-section switches with buffer layers of  $\text{TiO}_2$ . The leakage resistance of the  $\text{TiO}_2$  film is much lower than that of the  $\text{SiO}_2$  film. These switches work at dc which supports or at least is consistent with the above model. The switching response at 60 Hertz is shown in Figure 26. The



IF  $R_b \gg R_L$   $V_L \approx 0$  UNDER DC OPERATION ( $\text{SiO}_2$  OPERATION)

IF  $R_L \gg R_b$   $V_L \approx V_a$  UNDER DC OPERATION ( $\text{TiO}_2$  OPERATION)

Figure 25. Equivalent circuit model of  $\text{LiNbO}_3$ -buffer layer electrode configuration.

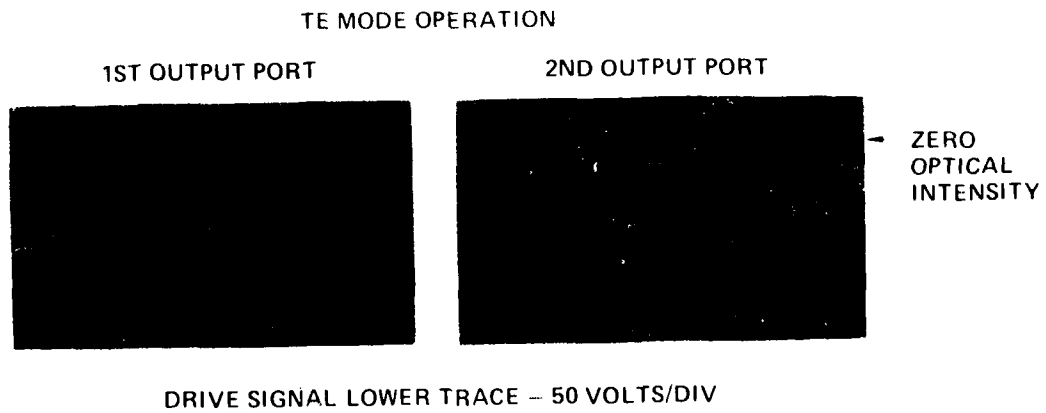


Figure 26. Four section switch operation at 60 Hertz.

switching states are obtained with 11 and 22 volts. Additional experiments are required to optimize the buffer layer.

#### D. AR COATING STUDY

In order to eliminate reflections from the interfaces between GaAlAs laser ( $n \sim 3.35$ ) fiber ( $n \sim 1.48$ ) and  $\text{LiNbO}_3$  ( $n \sim 2.2$ ) chips antireflection (AR) coatings can be placed between the components. Three coatings have been designed for the following interfaces:

- Laser/air/ $\text{LiNbO}_3$
- Fiber/ $\text{LiNbO}_3$
- Laser/Air/Fiber

Only the first two of these coatings have been deposited at HRL to date. For this program only the fiber to  $\text{LiNbO}_3$  coating has been studied.

The coating that we are investigating for the fiber  $\text{LiNbO}_3$  interface is illustrated in Figure 27. This coating requires no air gap. The AR coating was designed using the average refractive index of  $\text{LiNbO}_3$  at  $0.85 \mu\text{m}$  and a fiber index of 1.48. Figure 27 shows the resulting reflections for variations from these values. The coating is  $0.0975/0.0556 \lambda$  thickness of  $\text{ThF}_5/\text{ZnSe}$ . This coating has been deposited and tested; the result was a 0.1% reflection.

The only difficulty remaining is getting a consistent coating on the edge of the chip. The coating is being applied with a permanently attached end piece to protect the edge. During the deposition, the glue bond is out-gassing, causing the layer at the edge to be inconsistent with the remainder of the chip face. A special epoxy needs to be found that does not have this difficulty.

The experimental setup for the AR coating test is schematically shown in Figure 28. A fused multimode fiber 3 dB tee coupler was used. Light was launched into one branch of the fiber tee from a  $1.15 \mu\text{m}$  HeNe laser. The light reflected from the ends opposite the launch end of the coupler was then sampled (-3 dB sample) at the final port. The following measurements were made:



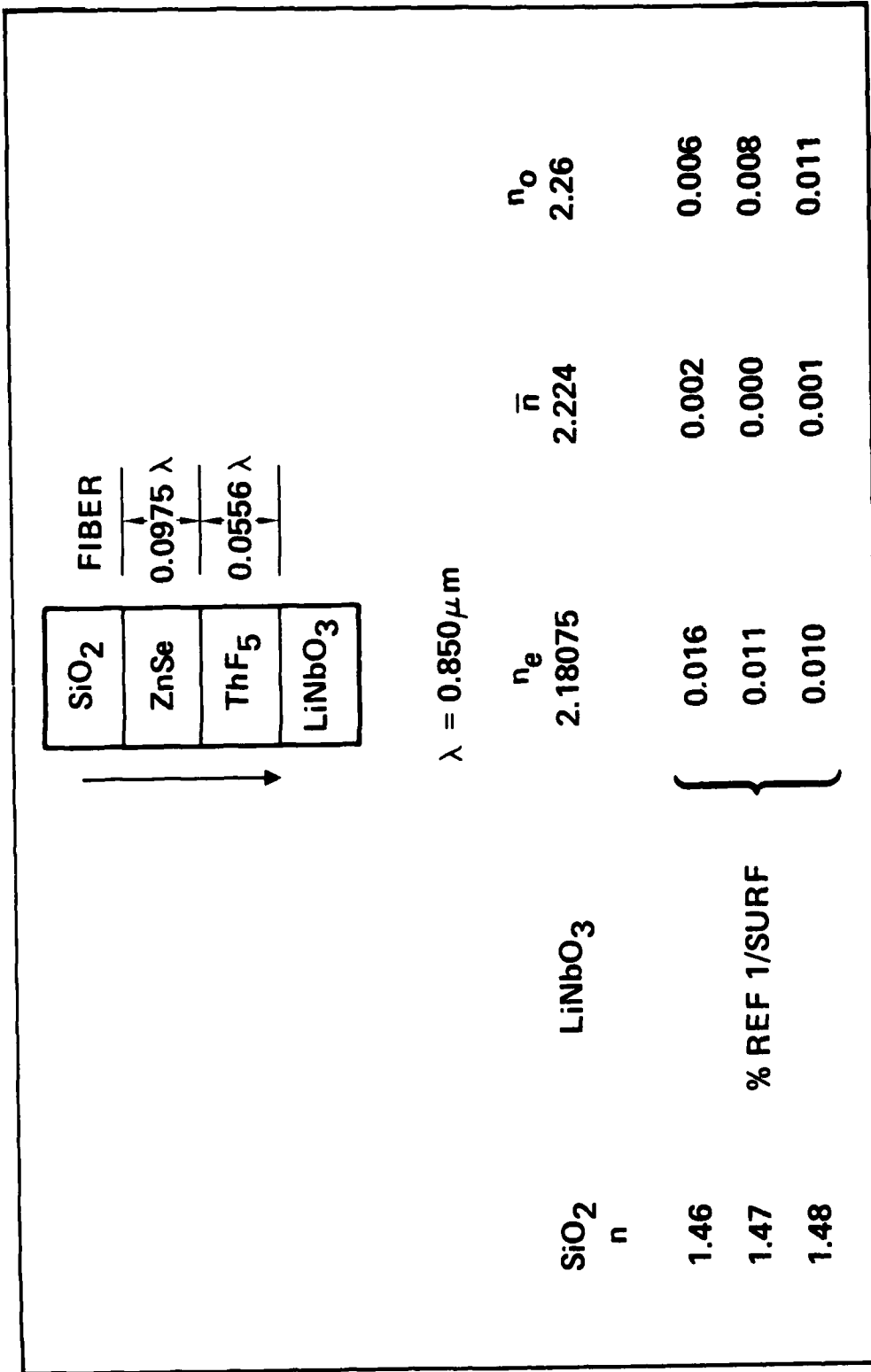


Figure 27. AR coating design.

- No excitation from laser (background) = .26 na
- Laser excitation bare fiber @ output end = 1.52 na  
(calibration measurement = 4% reflectance)
- Laser excitation output fibers against  $\text{LiNbO}_3$  but with air gap = 3.3 na
- Laser excitation output fibers against  $\text{LiNbO}_3$  with index matching liquid (designed configuration) = .3 na

From the background adjusted calibration and designed configuration measurements, the calculated/measured reflectance from the fiber  $\text{LiNbO}_3$  interface is .1%. This value is in good agreement with the expected reflectance.

#### E. OUTDIFFUSION ELIMINATION STUDIES

A problem in the fabrication of Ti diffused  $\text{LiNbO}_3$  waveguides is that, at high diffusion temperatures (850 to 1100°C), the  $\text{LiNbO}_3$  substrate suffers the loss of loosely bound  $\text{Li}_2\text{O}$  through a surface outdiffusion process. The deviation from crystal stoichiometry at the sample surface increases the extraordinary refractive index and leaves the ordinary refractive index unchanged.<sup>10</sup> As a result, there is a planar waveguide formed due to  $\text{Li}_2\text{O}$  outdiffusion in addition to the waveguide formed by metal indiffusion. In channel waveguide devices, the existence of the planar outdiffusion waveguide introduces excess crosstalk between channels and increases background noise of the devices. Furthermore, in an end-butt coupling configuration between a channel waveguide and a single mode optical fiber or a diode laser source, a significant amount of the optical energy is coupled to these unwanted outdiffusion modes. Recently, several authors have reported techniques to eliminate the  $\text{Li}_2\text{O}$  outdiffusion waveguide by indiffusion of  $\text{Li}_2\text{O}$  either during or after the Ti diffusion process. The  $\text{Li}_2\text{O}$  vapor derived from a  $\text{Li}_2\text{O}$  source,<sup>11</sup>  $\text{LiNbO}_3$  powder,<sup>12</sup> and  $\text{Li}_2\text{CO}_3$  powder,<sup>13</sup> is higher than the equilibrium vapor pressure so that the outdiffusion process from the  $\text{LiNbO}_3$  wafer is suppressed. At the same time, the compensation

process in which  $\text{Li}_2\text{O}$  is indiffused into a Li-deficient  $\text{LiNbO}_3$  wafer becomes thermodynamically favorable, Figure 29. In all cases, Ti-diffused planar waveguides were used to demonstrate the principle of indiffusion of  $\text{Li}_2\text{O}$ . However, for channel waveguides the same process that works well for Ti planar waveguides becomes critical in annealing temperature and annealing time. Most times, the same was either undercompensated or overcompensated. In the overcompensated samples the guide due to the Ti channel was also eliminated. Later, Burns,<sup>14</sup> et al., reported a successful compensation of nearly single mode Ti: $\text{LiNbO}_3$  channel waveguides using a modified  $\text{LiNbO}_3$  powder treatment. They concluded that the order of the treatments in  $\text{LiNbO}_3$  powder and in  $\text{O}_2$  is critical for channel compensation. It is believed in Ref. 8 that the indiffused  $\text{Li}_2\text{O}$  has to be redistributed to allow for the extraordinary mode propagation. In this study, we have tried to clarify some of the mystery involved in the  $\text{LiNbO}_3$  power compensation process. Experimental results reported here indicate that the index change associated with the Ti ions in  $\text{LiNbO}_3$  is dependent on the stoichiometry of the  $\text{LiNbO}_3$  wafer.

In the experimental study with channel waveguides, end fire coupling of a 1.15  $\mu\text{m}$  HeNe laser to the chips has been used. The technique we are using to eliminate the out diffusion is to do the Ti diffusion in an  $\text{Li}_2\text{O}$  atmosphere generated by placing the sample in a PT box containing  $\text{LiNbO}_3$  powder. Several Y-cut samples have been prepared and tested for modal properties. These samples differ in the amount of time diffused in the box, in  $\text{O}_2$ , and the order of diffusion in the two environments. All samples have guides of widths 5, 7, 9, 11 and 13  $\mu\text{m}$ . The initial depth of Ti was 500 Å. The samples and the associated designation are listed below.

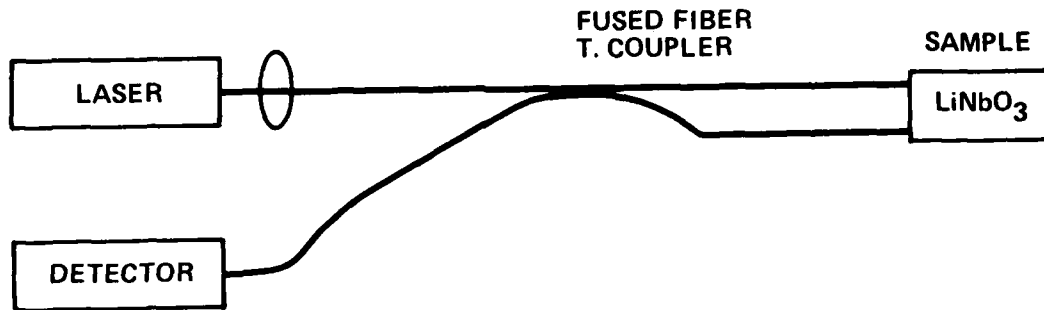


Figure 28. Schematic of experimental setup for the AR coating test.

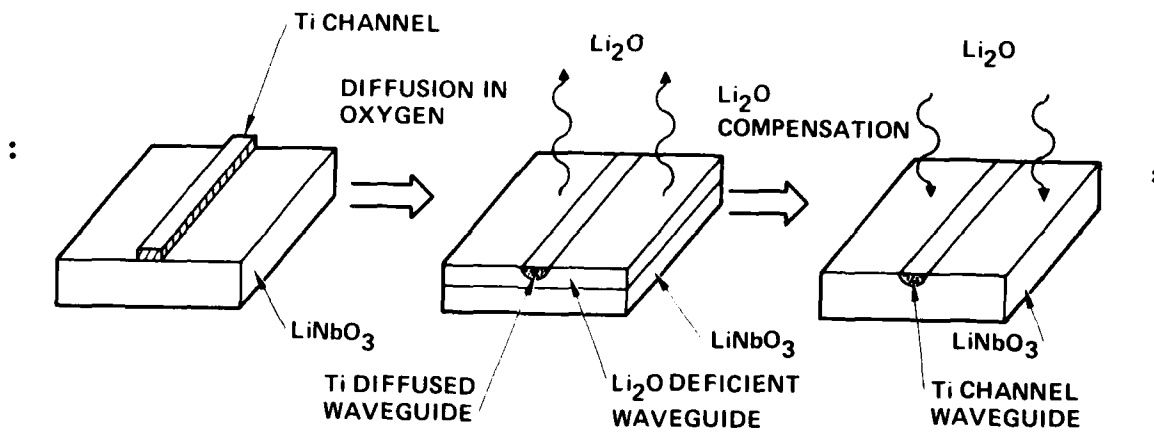


Figure 29. Elimination of outdiffused waveguides.

<u>Sample</u>	<u>Diffusions</u>
2-4 B	2 hrs box; 4 hrs O <sub>2</sub>
4-2 B	4 hrs box; 2 hrs O <sub>2</sub>
4-2 A	4 hrs O <sub>2</sub> ; 2 hrs box
2-4 A	2 hrs O <sub>2</sub> ; 4 hrs box
0-6 A	0 hrs O <sub>2</sub> ; 6 hrs box
6-2 B	6 hrs box; 2 hrs O <sub>2</sub>
6-6 A	6 hrs O <sub>2</sub> ; 6 hrs box
6-0 A	6 hrs O <sub>2</sub> ; 0 hrs box

The modal properties of these samples are summarized in Table 3. The following description is given to the code as used in the table.

CO Cut off

SM Single mode

HSM Halo single mode (i.e., approaching cut off with scattering producing a triangular halo extending above the guide into the substrate; throughput is still strong).

LSM Lossy single mode (i.e., very weak throughput and poor guide definition).

From the table, the presence or absence of excess Li<sub>2</sub>O in the crystal lattice has a strong effect upon the  $\Delta n$  produced by the Ti; with a lesser variation occurring in the ordinary index than the extraordinary index. The other effect suggested by the data is that waveguides supporting both polarizations can be obtained by an initial diffusion in LiNbO<sub>3</sub> powder followed by a diffusion in O<sub>2</sub> while samples supporting only the ordinary polarization can be obtained by an initial diffusion in O<sub>2</sub> followed by a diffusion in LiNbO<sub>3</sub>. It also suggests that the diffusion processing may be used to optimize devices. More experiments are required before we can determine a process for device development using the r33 electrooptic coefficient. Experiments involving both Y and Z cut LiNbO<sub>3</sub> are required to establish the optimum configuration and process. Some of these experiments are presently under way with IR&D funds.

Table 3. Properties of Samples  $\text{Li}_2\text{O}$  Outdiffusion Elimination

Sample	5 $\mu\text{m}$		7 $\mu\text{m}$		9 $\mu\text{m}$		11 $\mu\text{m}$		13 $\mu\text{m}$	
	TE	TM	TE	TM	TE	TM	TE	TM	TE	TM
2-4B	CO	CO	CO	CO	HSM	HSM	SM	SM	SM	SM
4-2B	CO	CO	CO	CO	HSM	SM	SM	SM	MM	SM
4-2A	CO	CO	CO	SM	CO	SM	LSM	SM	LSM	MM
2-4A	CO	CO	CO	HSM	LSM	SM	LSM	SM	HSM	SM
0-6A	CO	CO	CO	CO	CO	CO	CO	CO	CO	LSM
6-2B	CO	CO	CO	CO	CO	CO	LSM	HSM	HSM	HSM
6-6A	CO	CO	CO	LSM	LSM	SM	SM	SM	SM	SM
6-0A	SM	CO	SM	CO	MM	SM	MM	SM	MM	SM

CO Cut off  
 SM Single mode  
 MM Multimode  
 HSM Halo single mode (see text)  
 LSM Observed but very weak (i.e., lossy single mode)

## SECTION 3

### DELIVERABLE TEST RESULTS

#### A. INTRODUCTION

Hughes Aircraft has conducted a research and development effort resulting in the demonstration and delivery of an integrated optic switch permanently attached to fiber pigtails. The switch operates at  $.85 \mu\text{m}$  with a throughput loss of 7.8 dB from fiber-to-chip-to-fiber; a value close to the theoretical optimum. The switch is electronically switchable with switching voltages for the T.E. polarization of 25 volts for the cross state and 50 volts for the parallel state. These are higher than reported for a similar switch in Section 2c; this is believed due to a thick  $\text{SiO}_2$  layer. The switch does not operate at dc due to the buffer layer being  $\text{SiO}_2$  (see Section 2c). In the following paragraphs, we will compare switch operation with statement of work goals. The organization is that each numbered subsection is a program goal. In each subsection we summarize the experimental and theoretical results that apply to that goal.

#### B. PROGRAM GOALS AND RESULTS

##### 1. Insertion Loss

The insertion loss, i.e., the loss induced in a single mode, reference fiber which represents the gyro or delay line loop, by the presence of the coupler shall be less than 1 dB.

With reference to Figure 30; this requires that the loss from point B to point D be less than 1 dB; this however is not believed possible with the present approach. The losses from point B to D are equivalent to the losses from B to C or A to D. These losses are summarized in the next section. A complete discussion is found in Section 2.

## 2. Coupling Loss in on Position

The coupling loss from the external fiber through the coupler to the reference fiber shall be less than 3 dB while the coupler is in the on position.

In reference to Figure 30, this requires that the losses from point A to D or B to C be less than 3 dB. The deliverable has a loss of 7.8 dB under these conditions. This total loss can be divided in the following way:

- 2.5 dB propagation attenuation (chip ~2.5 cm in length)
- 1 dB bends and offsets
- .35 dB reflections due to lack of AR coating
- 3.9 dB fiber-to-chip coupling loss.

The 3 dB value probably cannot be achieved with a switch of this configuration. The fiber-to-chip coupling loss can be reduced to about 2 dB. The bend and offset loss is also presently limited by mask making capabilities, but fundamentally can be reduced to ~.35 dB by eliminating the offset errors at waveguide intersections; this remaining .35 dB is due to the bends. The attenuation may decrease with increased wavelength due to reduced scattering, but this has not been confirmed. This will not be the case if the primary loss is absorption instead of scattering. The total chip length can be reduced and maintain low switching voltages by designing the switch for TM operation instead of TE. This could result in a 1 dB reduction in the propagation loss.

## 3. Coupling Loss in off Position

The coupling loss from the external fiber through the coupler to the reference fiber shall be greater than 30 dB while the coupler is in the off position.

This particular specification is a crosstalk requirement when the switch is in a bar state. The switching curves for the deliverable are displayed in Figure 31. This photo shows three traces from the



10353--5

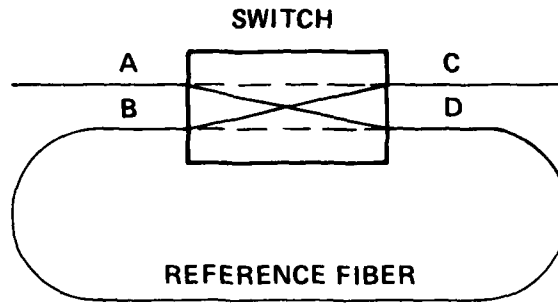


Figure 30.  
Schematic diagram of a switch system.

10353-4

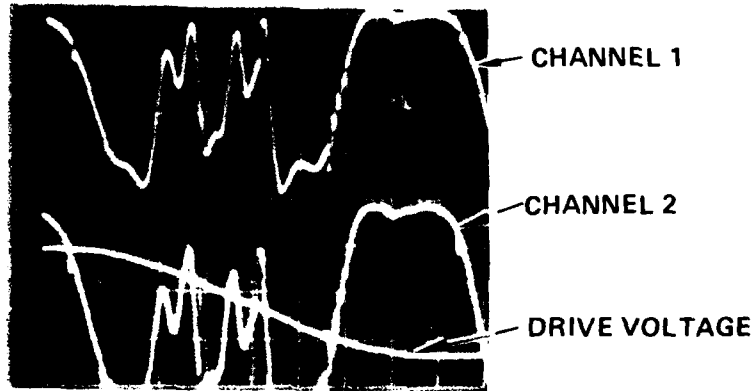


Figure 31.  
Switching curves for the deliverable shown are the drive voltage at 50 V/division and the output of the two channels.

oscilloscope. First is the drive voltage (60 cycles @ 50 volts/div.). The other two traces are the detected intensities at the fiber outputs. These intensity levels are exact images of each other. For both traces, zero optical intensity is at the center of the scope. For the top trace, increased intensity goes up; for the bottom trace, increased intensity goes down. From these photographs, we can see approximately a 20 dB crosstalk ratio at both the bar and cross states. This level is strongly dependent on the input polarization as the polarizations respond differently to the applied voltage. For a two section switch with no buffer layer, the crosstalk versus time for the cross state is shown in Figure 32. This shows that the 30 dB requirement can indeed be realized. The drift with time measured can be eliminated by pulsed operation or by maintaining a zero mean bias.

#### 4. Reflections

Reflections in the reference fiber from the coupler shall be down at least 30 dB while the coupler is in the off position.

The reflections can be reduced to this level (see Section 2) however, in the deliverable, the AR coating was not applied due to the difficulties reported earlier. The reflections in the deliverable are only down by 14 dB.

#### 5. Time Response

The time for the coupler to be in the on position shall be variable over the range from 2 to 4  $\mu$  secs/pulse. The rise and fall time for the switchable coupler shall be less than 200 nanoseconds. Techniques used shall not preclude the coupler being used for on-times longer than 4  $\mu$  seconds.

Switches similar to the one delivered have demonstrated GHz modulation bandwidths and nanosecond response times to pulses. The experimental data shown in Figure 33 is not limited by the pulse response of the switch, but by the source; however, the requirements for the rise-time

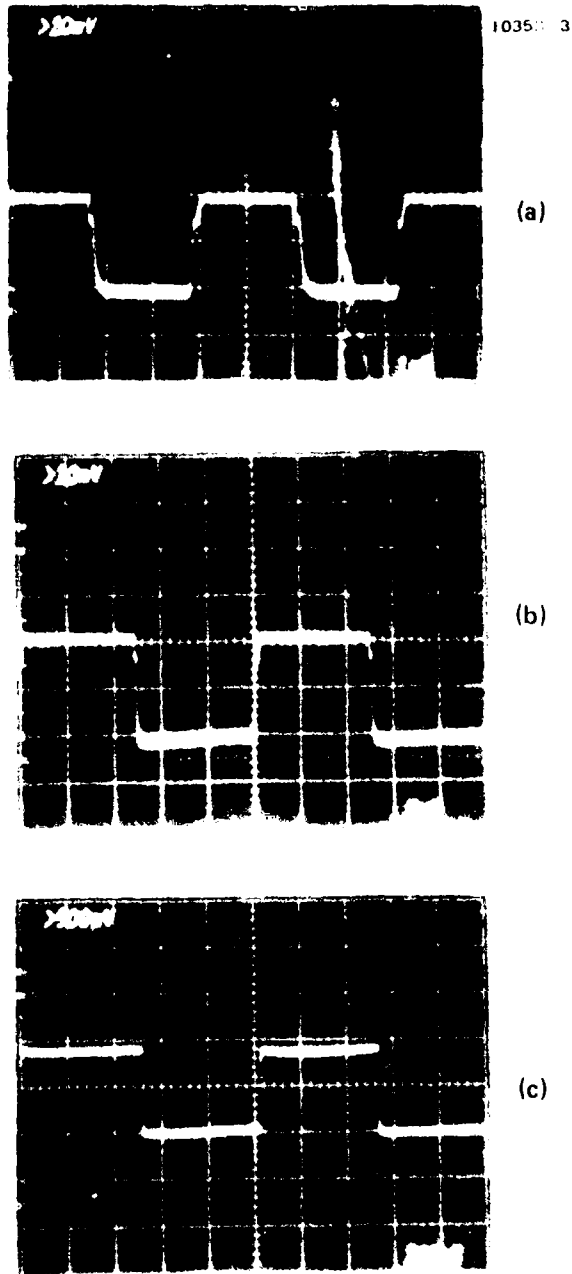


Figure 32.  
 Experimental data showing the rise and fall time of the delivered switch and pulsed operation varying between (a) 2  $\mu$ sec; (b) 4  $\mu$ sec; (c) 500  $\mu$ sec.

above are clearly demonstrated. The on-time requirements of 2 to 4 usecs/pulse are clearly demonstrated in Figures 32a and b. The requirement for potentially longer on-times is demonstrated in Figure 32c where an on-time of 500 usec is indicated.

#### 6. Repetition Rate

The repetition rate for the switchable coupler shall be adjustable from  $0.1 \times 10^3$  to  $25 \times 10^3$  pulses per second.

Once the buffer layer problem has been completely investigated and a procedure is established to give dc operation of switches with low loss, the lower end of these requirements will be feasible. Presently, with this long of a pulse or dwell time, there is some drift in the optical crosstalk. This is shown in Figure 33. Here the electrical pulse and the detected optical pulse are displayed. The pulse-widths are 2 msec and the drift in the optical pulse is clear. This is not believed to be a fundamental problem.

#### 7. Wavelength

Ultimate operating wavelengths desired will be from 1.06 to 1.3  $\mu\text{m}$ . For this work statement feasibility was demonstrated at .83  $\mu\text{m}$ .

The work required to achieve the desired wavelength of operation is discussed in detail in the Recommendation and Conclusions section of this report. Basically, the following will be entailed:

- Experimental fiber-to-chip coupling followed by
- Experimental chip optimization by varying interaction length and electrodes, electrooptic coefficient or polarizaton
- AR coating development
- Buffer layer optimization.

10353-2

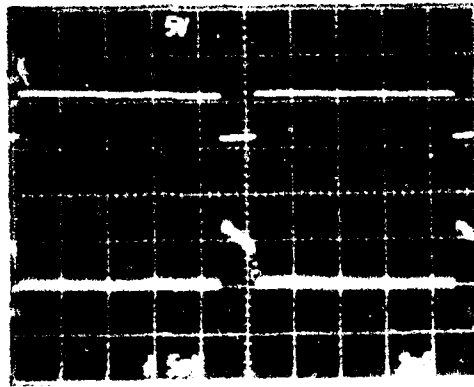


Figure 33.  
Experimental data showing optical  
amplitude pulse drift. The drive  
pulse is provided as a reference.

8. Pigtails

The coupler operation was demonstrated to and from a single mode fiber. A photograph of the deliverable is shown in Figure 34.



Figure 34. Photograph of deliverable illustrating single mode fibers and switch.

## SECTION 4

### RECOMMENDATIONS AND CONCLUSIONS

#### A. INTRODUCTION

This highly successful program has resulted in the demonstration of a low-loss, low voltage, high speed switchable directional coupler with single mode fiber pigtailed. Although the overall loss of the device is approaching theoretical limits, there are some areas where obvious improvements are required. Before discussing these areas, the accomplishments of this program are summarized below:

- Demonstrated two- and four-section  $\Delta\beta$  reversal switches at  $.85 \mu\text{m}$ . Recently under another program a four-section switch was demonstrated at  $1.06 \mu\text{m}$ .
- Demonstrated less than 1 dB coupling loss between  $\text{LiNbO}_3$ :Ti-diffused strip waveguides and single mode fibers.
- Assembled electrooptic directional coupler switch with permanently attached single mode fibers, fiber-to-chip coupling losses of  $\sim 1.8$  dB, and total fiber-to-chip-to-fiber loss of 7.8 dB. Chip contained a four-section  $\Delta\beta$  reversal switch and was 2.5 cm in length. There were four attached fiber pigtailed.
- Demonstrated successfully the deposition of the buffer layers between waveguides and electrodes.
- Demonstrated consistent, flat, and chip-free edge polishing.
- Demonstrated AR coatings for the interfaces between  $\text{LiNbO}_3$  chip and fibers.
- Analyzed losses associated with bends and offsets in waveguides confirmed analysis with experimental data.
- Demonstrated  $\text{Li}_2\text{O}$  outdiffusion mode elimination.



Based on this extensive work we recommend that additional research be conducted on the following:

- Deposited AR coatings on chip edges.
- Study buffer layers that will allow switch operation at dc.
- Continued studies to eliminate  $\text{Li}_2\text{O}$  outdiffusion mode problems to optimize the switching voltages.
- Fiber coupler fixture optimization.
- Optimization of fiber-to-waveguide coupling at longer wavelengths.
- Optimization of switches with the optimum waveguides and electrode arrangement at longer wavelengths.

The first 3 topics have been discussed in detail in Section 2. The last three are discussed below.

#### B. FIBER COUPLER FIXTURE OPTIMIZATION

After both pair of input and output fibers were attached to the device shown in Figure 34 we adjusted the fibers by maximizing the total throughput into the output fibers with both input fibers excited. The total throughput loss on the deliverable was 7.8 dB. After subtracting circuit losses and propagation losses, the remaining 3.9 dB is associated with the fiber-to-chip coupling. This larger than expected coupling loss is believed to be associated with the precision with which we can position the fibers using the present fixture or possibly the concentricity of the fiber core. This conclusion is based on the following observations. First, the total throughput was maximized as described above. After blocking either laser source, the remaining throughput could with adjustment of the fibers then be increased by ~10%. Unblocking of the second laser source then resulted in a decreased total throughput. These results can be attributed to either a lack of precision in the angular alignment of the fibers or the lack

of concentricity of the fiber cores. Experiments need to be conducted to establish the nature of the difficulty. If it is angular alignment, more care is required in the assembly process. If it is the fiber core concentricity, then we will have to establish a test to ensure the fiber core to fiber core separation of 110  $\mu\text{m}$ .

#### C. FIBER-TO-WAVEGUIDE COUPLING @ 1.06 - 1.3 $\mu\text{m}$

The majority of the research conducted during this program was done at .8 - .85  $\mu\text{m}$ ; however, our initial goal was to make the device for the 1.15  $\mu\text{m}$  HeNe line. The primary reason for the .85  $\mu\text{m}$  research is the current lack of a commercially available single mode fiber at 1.15  $\mu\text{m}$ . Initially we believed that the ITT 4.5  $\mu\text{m}$  core fiber would support the 1.15  $\mu\text{m}$  mode with low loss; however, we found that any bend in the fiber caused excessive loss. A fiber obtained from Bell Laboratories supported the 1.15  $\mu\text{m}$  mode; however, we felt it would be fruitless to do the research with a one-of-a-kind fiber. Prior to making the decision to pursue a .85  $\mu\text{m}$  device and prior to perfecting our fiber and  $\text{LiNbO}_3$  polishing techniques, losses of about 2.5 dB were observed between Bell fiber and channel waveguides at 1.15  $\mu\text{m}$ . This Bell fiber has a core diameter of 8  $\mu\text{m}$ . Any fiber for the longer wavelength will have a larger core than the ITT fiber; but the core should be kept as small as possible to optimize the fiber-to-channel waveguide coupling; a core diameter of 6-7  $\mu\text{m}$  is believed to be optimum.

The experiments required to optimize the coupling between single mode fiber and channel waveguides at 1.15 or any wavelength between 1.06 and 1.3  $\mu\text{m}$  are similar in nature to those conducted during this program at .83  $\mu\text{m}$ . It is expected that the coupling losses will be larger and the optimum will be more clearly defined since we will not be working in the  $W/D \approx 2$  region of the diffusion curve (see Figure 14 and associated discussion). These experiments will probably be conducted after the single mode fiber is available commercially or fabricated at HRL.

#### D. SWITCH OPTIMIZATION FOR THE LONGER WAVELENGTH

Once the Ti source depth and diffusion parameters are established for the optimum fiber-to-guide coupling at the wavelength of operation, the coupling length will have to be determined in order to design a switch mask. The technique for determining the coupling length has been discussed in Section 2.

At the longer wavelength, the circuit losses, except for the bend loss which scales as (waist/wavelength), will probably be lower. The propagation loss especially will be reduced if the primary loss is due to scattering.

At the longer wavelength, the switching voltages will be increased if the same number of sections and overall length is maintained. Possible techniques of reducing the switching voltages are presently being investigated with IR&D funds.

Switch development at the 1.06  $\mu\text{m}$  wavelength is presently being conducted for the British Aerospace Corporation (BAS). No fiber pigtails are required for this program. The switch developed for BAS will serve as a test bed for on-chip losses at 1.06  $\mu\text{m}$ .

#### REFERENCES

1. W.C. Goss, R. Goldstein, M.D. Nelson, H.T. Fearnhaugh, and O.G. Ramer, *Appl. Opt.* 19, 852 (1980).
2. H. Kogelnik and R.V. Schmidt, *IEEE J. Quantum Electronics* QE-12, 396 (1976).
3. J.F. Nye, *Physical Properties of Crystals* (Oxford at the Clarendon Press, London, 1957).
4. R.J. Pressley (Ed), *Handbook of Lasers* (Chemical Rubber Company, Cleveland, 1971).
5. E. Marcatili, *Bell System Tech. J.* 48, pp 2071-2102, (1969).
6. R.V. Schmidt, and R.C. Alferness, *IEEE Transactions on Circuits and Systems*, CAS-26, 12, 1099 (1979).
7. W.K. Burns and G.B. Hocker, *Appl. Opt.* 16, 2048 (1977).
8. L.G. Cohen, *Bell Syst. Tech. J.*, 573 (1972).
9. J. Noda, O. Mikami, M. Minakata and M. Fakuma, *App. Optics*, 17, 2092 (1978).
10. J.R. Carruthers, G.E. Peterson, M. Crasso and P.M. Bridenbaugh, *J. Appl. Phys.* 42, 1846 (1971).
11. T.R. Ranganath and S. Wang, *Appl. Phys. Lett.* 30, 376 (1977).
12. B. Chen and A.C. Pastor, *Appl. Phys. Lett.* 30, 570 (1977).
13. S. Miyazawa, R. Guglielmi and A. Carencio, *Appl. Phys. Lett.* 31, 742 (1977).
14. W.K. Burns, C.H. Bulmer and E.J. West, *Appl. Phys. Lett.* 33, 70 (1978).

## APPENDIX

### ANALYSIS OF BENDS AND OFFSET LOSSES IN INTEGRATED OPTIC CHANNEL WAVEGUIDES

#### I. INTRODUCTION

The coupling of modes at an interface is given by the overlap integral between the modes. This is expressed by:

$$\epsilon = \frac{\left| \int_{-\infty}^{\infty} \int_{-\infty}^{\infty} \psi_1 \psi_2^* dx dy \right|^2}{\int_{-\infty}^{\infty} \int_{-\infty}^{\infty} \psi_1 \psi_1^* dx dy \int_{-\infty}^{\infty} \int_{-\infty}^{\infty} \psi_2 \psi_2^* dx dy} \quad \text{A1}$$

where  $\psi_1$  and  $\psi_2$  are the amplitude functions for the two modes. In the analysis, the y coordinate axis is normal to the film and no modal variation is assumed along this axis; therefore

$$\epsilon = \frac{\left| \int_{-\infty}^{\infty} \psi_1 \psi_2^* dx \right|^2}{\int_{-\infty}^{\infty} \psi_1 \psi_1^* dx \int_{-\infty}^{\infty} \psi_2 \psi_2^* dx} \quad \text{A2}$$

#### II. GAUSSIAN ANALYSIS

For simplicity we will initially consider a simple case of Gaussian mode profiles then consider the waveguide analysis of Marcatili<sup>5</sup> and the associated mode profiles. It should be pointed out however that the Gaussian analysis is not completely general since part of the Gaussian z-dependent phase terms have been neglected. The analysis therefore only applies within the waist of the Gaussian beam or for a hypothetical guided Gaussian that is not allowed to expand. We assume

$$\psi_1 = e^{-\left(\frac{x_1}{\omega}\right)^2 - i k z_1} \quad \text{A3}$$

and

$$\psi_2 = e^{-\left(\frac{x_2}{\omega}\right)^2 - i k z_2} \quad \text{A4}$$

consider first the geometry shown in Figure 22 which is a waveguide with an angular bend,  $\theta$ . For this situation, we can write

$$x_1 = x_2 \cos \theta - z_2 \sin \theta \quad \text{A5}$$

$$z_1 = x_2 \sin \theta + z_2 \cos \theta \quad \text{A6}$$

or by assuming  $z_1 = 0$

$$x_2 = x_1 \cos \theta \quad \text{A7}$$

$$z_2 = -x_1 \sin \theta \quad \text{A8}$$

Upon substitution into Eqs. A3-A4 and assuming  $\theta$  is small, we have

$$\psi_1 = e^{-\left(\frac{x_1}{\omega}\right)^2} \quad \text{A9}$$

$$\psi_2 = e^{-\left(\frac{x_1}{\omega}\right)^2 + i k x_1 \sin \theta} \quad \text{A10}$$

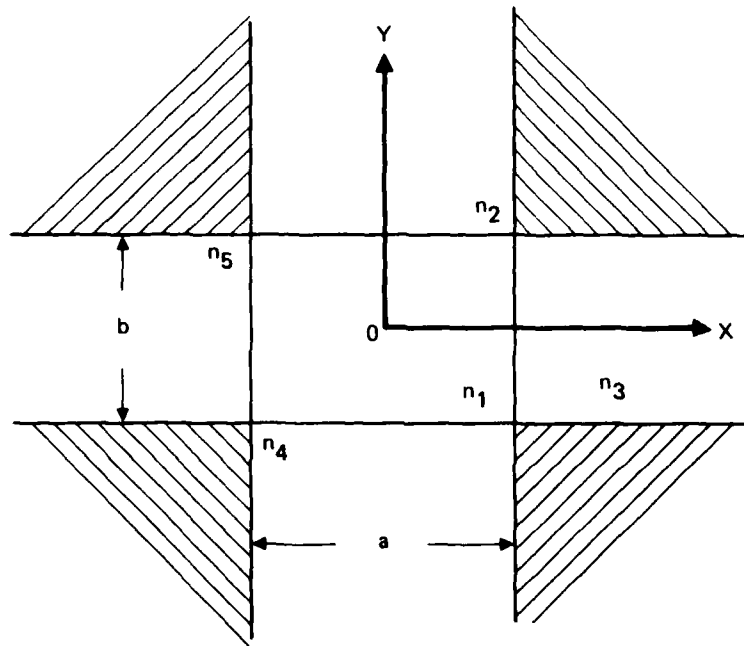


Figure A-1. Geometry of a rectangular dielectric waveguide. The field in the shaded regions is ignored in the approximation.

Substitution of this into Eq. A2 and doing the integrals gives

$$\epsilon = e^{-\left(k^2 w^2 \sin^2 \theta / 4\right)} \quad \text{A11}$$

Some dependencies should be pointed out:

- For a given  $w$ , the loss will decrease for increase in wavelength,  $\lambda$ .
- For a given  $\lambda$ , the loss will increase for an increase of the Gaussian waist  $w$ .
- For a given ratio  $w/\lambda$  these losses remain constant.

The second geometry to consider is shown in Figure 23. For this case  $z_1 = z_2 = 0$  and  $x_1$  and  $x_2 + \delta$ ; therefore

$$\psi_1 = e^{-\left(\frac{x_1}{w}\right)^2} \quad \text{A12}$$

$$\psi_2 = e^{-\frac{1}{2} \left(\frac{x_1 - \delta}{w}\right)^2} \quad \text{A13}$$

Upon substitution into Eq. A2 and doing the integrals, we obtain

$$\epsilon = e^{-\left(\frac{\delta}{w}\right)^2} \quad \text{A14}$$

In this case

- The losses increase with increasing  $\delta$
- The losses decrease with increasing mode width.



### III. MARCATILI ANALYSIS

In the Marcatili<sup>5</sup> analysis, a waveguide immersed in several dielectrics as shown in Figure A1 was considered. In this analysis the actual waveguide parameters can be substituted. The guide has a width of  $a$  along the  $x$  axis, a height of  $b$  along  $y$  axis, and a direction of propagation that is parallel to the  $z$  axis. Since an exact solution of the problem is not possible, approximations are made in the analysis to obtain a closed-form solution.

As shown in Figure A1, we will neglect the power that travels through the shaded regions and the fields need only be matched along the boundaries of Region 1. There are two sets of modes that satisfy the boundary conditions,  $E_{pq}^x$  and  $E_{pq}^y$ .  $E_{pq}^x$  modes, with dominant electric field polarized in the  $x$  direction, have field components  $E_x, E_y = 0, E_z, H_x = 0, H_y$ , and  $H_z$ .  $E_{pq}^y$  modes, on the other hand, have electric field polarized along the  $y$  direction and with field components  $E_y, E_x = 0, E_z, H_x, H_y = 0$ , and  $H_z$ .  $E_{pq}^x$  modes are similar to the TE modes of a slab waveguide, and  $E_{pq}^y$  modes resemble the TM modes.

If we assume that all the field components have a time and  $z$  dependence of the form  $e^{i(\omega t - k_z z)}$ , then Maxwell's equations can be written as

$$\nabla_x \bar{E} = -i \mu_0 \bar{H}$$

$$\nabla_x \bar{H} = i \epsilon \bar{E}$$

From these equations, all the transverse field components  $E_x, E_y, H_x$ , and  $H_y$  can be expressed in terms of the longitudinal components  $E_z$  and  $H_z$ :

$$\begin{aligned}
E_x &= -\frac{i}{K_v^2} \left( \beta \frac{\partial E_z}{\partial x} + \omega \mu_0 \frac{\partial H_z}{\partial y} \right) \\
E_y &= -\frac{i}{K_v^2} \left( \beta \frac{\partial E_z}{\partial y} - \omega \mu_0 \frac{\partial H_z}{\partial x} \right) \\
H_x &= -\frac{i}{K_v^2} \left( \beta \frac{\partial H_z}{\partial x} - \omega \epsilon_0 n_v^2 \frac{\partial E_z}{\partial y} \right) \\
H_y &= -\frac{i}{K_v^2} \left( \beta \frac{\partial H_z}{\partial y} + \omega \epsilon_0 n_v^2 \frac{\partial E_z}{\partial x} \right) ,
\end{aligned}$$

where

$$K_v^2 = n_v^2 k^2 - k_z^2, \text{ and } k^2 = \omega^2 \mu_0 \epsilon_0 .$$

The refractive index  $n_v$  assumes the values  $n_1, n_2, n_3, n_4,$  and  $n_5$  for fields in the five regions of the waveguide. Both  $E_z$  and  $H_z$  must satisfy the following reduced wave equation:

$$\frac{\partial^2}{\partial x^2} \begin{pmatrix} E_z \\ H_z \end{pmatrix} + \frac{\partial^2}{\partial y^2} \begin{pmatrix} E_z \\ H_z \end{pmatrix} + K_v^2 \begin{pmatrix} E_z \\ H_z \end{pmatrix} = 0$$

Since  $E_z$  and  $H_z$  are independent, we can choose their amplitude coefficients such that either  $H_x = 0$  or  $H_y = 0$ . If  $H_x = 0$ , the set of solutions will make up the  $E_{pq}^x$  modes; if  $H_y = 0$ , it will make up the  $E_{pq}^y$  modes.

1.  $E_{pq}^x$  Modes: Polarization Along x

The field components in the  $v$ -th region are

$$E_{xv} = e^{i(\omega t - k_z z)} \left\{ \begin{array}{l} M_1 \cos(k_x x + \alpha) \cos(k_y y + \beta) \quad v = 1 \\ M_2 \cos(k_x x + \alpha) e^{-k_y y} \quad v = 2 \\ M_3 \cos(k_y y + \beta) e^{-k_x x} \quad v = 3 \\ M_4 \cos(k_x x + \alpha) e^{-k_y y} \quad v = 4 \\ M_5 \cos(k_y y + \beta) e^{-k_x x} \quad v = 5 \end{array} \right. \quad A15$$

$$E_y = 0$$

$$E_{zv} = -\frac{1}{k_z} \frac{\partial E_x}{\partial x}$$

$$H_{xv} = 0$$

$$H_{yv} = \frac{1}{\mu_0 k_z} \left( k_z^2 - \frac{\omega^2}{c^2} \right) E_{xv}$$

$$H_{zv} = -\frac{i}{\mu_0} \frac{\partial E_x}{\partial y}$$

$$k_x^2 + k_y^2 + k_z^2 = k^2 n_1^2$$

$$k_x^2 - k_y^2 + k_z^2 = k^2 n_2^2$$

$$-k_x^2 + k_y^2 + k_z^2 = k^2 n_3^2$$

$$k_x^2 - k_y^2 + k_z^2 = k^2 n_4^2$$

$$-k_x^2 + k_y^2 + k_z^2 = k^2 n_5^2$$

A16

The boundary conditions require that the tangential components of E and H be continuous at all boundaries:

$$E_{x1} = E_{x2} \quad , \quad H_{z1} = H_{z2} \quad y = \frac{b}{2}$$

$$E_{x1} = E_{x4} \quad , \quad H_{z1} = H_{z4} \quad y = -\frac{b}{2}$$

$$E_{z1} = E_{z3} \quad , \quad H_{y1} = H_{y3} \quad x = \frac{a}{2}$$

$$E_{z1} = E_{z5} \quad , \quad H_{y1} = H_{y5} \quad x = -\frac{a}{2}$$

quating these field components gives

$$\begin{cases} M_1 \cos\left(\frac{k_y b}{2} + \delta\right) = M_2 e^{-\frac{k_y b}{2}} \\ M_1 \cos\left(-\frac{k_y b}{2} + \delta\right) = M_4 e^{-\frac{k_y b}{2}} \end{cases} \quad \text{A17}$$

$$\begin{cases} -M_1 k_y \sin\left(\frac{k_y b}{2} + \beta\right) = -M_2 k_{y2} e^{-\frac{k_{y2} b}{2}} \\ -M_1 k_y \sin\left(-\frac{k_y b}{2} + \beta\right) = M_4 k_{y4} e^{-\frac{k_{y4} b}{2}} \end{cases} \quad \text{A18}$$

$$\begin{cases} -M_1 k_x \sin\left(\frac{k_x a}{2} + \alpha\right) = -M_3 k_{x3} e^{-\frac{k_{x3} a}{2}} \\ -M_1 k_x \sin\left(-\frac{k_x a}{2} + \alpha\right) = M_5 k_{x5} e^{-\frac{k_{x5} a}{2}} \end{cases} \quad \text{A19}$$

$$\begin{cases} (k_z^2 + k_x^2) M_1 \cos\left(\frac{k_x a}{2} + \alpha\right) = (k_z^2 - k_{x3}^2) M_3 e^{-\frac{k_{x3} a}{2}} \\ (k_z^2 + k_x^2) M_1 \cos\left(-\frac{k_x a}{2} + \alpha\right) = (k_z^2 - k_{x5}^2) M_5 e^{-\frac{k_{x5} a}{2}} \end{cases} \quad \text{A20}$$

From Eqs. A17 and A18, we have

$$\begin{cases} \tan\left(\frac{k_y b}{2} + \beta\right) = \frac{k_{y2}}{k_y} \\ \tan\left(\frac{k_y b}{2} - \beta\right) = \frac{k_{y4}}{k_y} \end{cases} \quad \text{A21}$$

From Eqs. A19, A20, and A21, we have

$$\begin{aligned} \tan\left(\frac{k_x a}{2} + \alpha\right) &= \left(\frac{k_{x3}}{k_x}\right) \left(\frac{k_z^2 + k_x^2}{k_z^2 - k_{x3}^2}\right) = \left(\frac{k_{x3}}{k_x}\right) \left(\frac{k^2 n_1^2 - k_y^2}{k^2 n_3^2 - k_y^2}\right) \\ \tan\left(\frac{k_x a}{2} - \alpha\right) &= \left(\frac{k_{x5}}{k_x}\right) \left(\frac{k_z^2 + k_x^2}{k_z^2 - k_{x5}^2}\right) = \left(\frac{k_{x5}}{k_x}\right) \left(\frac{k^2 n_1^2 - k_y^2}{k^2 n_5^2 - k_y^2}\right) \end{aligned} \quad \text{A22}$$

For modes well above cutoff,

$$k_z \approx n_1 k \text{ and } k \approx k_x, k_y ;$$

thus, Eq. A20 can be further reduced to

$$\begin{cases} \tan\left(\frac{k_x a}{2} + \alpha\right) = \frac{n_1^2}{n_3^2} \frac{k_{x3}}{k_x} \\ \tan\left(\frac{k_x a}{2} - \alpha\right) = \frac{n_1^2}{n_5^2} \frac{k_{x5}}{k_x} \end{cases} \quad \text{A23}$$

If we rewrite Eq. A21 as

$$\tan\left(\frac{k_y b}{2} + \beta\right) = \frac{k_{y2}}{k_y}$$

or

$$\tan\left[\frac{\pi}{2} - \left(\frac{k_y b}{2} + \beta\right)\right] = \frac{k_y}{k_{y2}} ,$$

then

$$\frac{\pi}{2} = \left( \frac{k_y b}{2} + \beta \right) = \tan^{-1} \frac{k_y}{k_{y2}} + m\pi \quad . \quad \text{A24}$$

Similarly,

$$\frac{\pi}{2} - \left( \frac{k_y b}{2} - \beta \right) = \tan^{-1} \frac{k_y}{k_{y4}} + n\pi \quad . \quad \text{A25}$$

Then sum of Eqs. A24 and A25 gives

$$\begin{aligned} \pi \dots k_y b &= (m + n) \pi + \tan^{-1} \frac{k_y}{k_{y2}} \\ &\quad + \tan^{-1} \frac{k_y}{k_{y4}} \end{aligned}$$

or

$$k_y b = q\pi - \tan^{-1} \frac{k_y}{k_{y2}} - \tan^{-1} \frac{k_y}{k_{y4}} \quad . \quad \text{A26}$$

Likewise, from Eq. A23 we have

$$k_x a = p\pi - \tan^{-1} \left( \frac{n_3^2}{n_1^2} \frac{k_x}{k_{x3}} \right) - \tan^{-1} \left( \frac{n_5^2}{n_1^2} \frac{k_x}{k_{x5}} \right) \quad \text{A27}$$

Eq. A16 can be rearranged to give the following relations:

$$k_{x3,5} = \left\{ \left( \frac{2\pi}{\lambda} \right)^2 (n_1^2 - n_{3,5}^2) - k_x^2 \right\}^{1/2}$$

$$k_{y2,4} = \left\{ \left( \frac{2\pi}{\lambda} \right)^2 (n_1^2 - n_{2,4}^2) - k_y^2 \right\}^{1/2}$$

$$k_z = \left\{ k_{n_1}^2 - k_x^2 - k_y^2 \right\}^{1/2}$$

Define the parameters  $\Lambda_{3,5}$  and  $\Lambda_{2,4}$  such that

$$\begin{aligned} \Lambda_{3,5} &= \frac{1}{k_{x3,5}} = \frac{1}{\left\{ \left[ \left( \frac{2\pi}{\lambda} (n_1^2 - n_{3,5}^2) \right)^{1/2} \right]^2 - k_x^2 \right\}^{1/2}} \\ &= \frac{1}{\left[ \left( \frac{\pi}{\Lambda_{3,5}} \right)^2 - k_x^2 \right]^{1/2}} \end{aligned}$$

where

$$\Lambda_{3,5} = \frac{\lambda}{2(n_1^2 - n_{3,5}^2)^{1/2}}$$

and

$$\Lambda_{2,4} = \frac{1}{k_{y2,4}} = \frac{1}{\left\{ \left[ \left( \frac{2\pi}{\lambda} (n_1^2 - n_{2,4}^2) \right)^{1/2} \right]^2 - k_y^2 \right\}^{1/2}} \left[ \left( \frac{\pi}{\Lambda_{2,4}} \right)^2 - k_y^2 \right]^{1/2},$$



with

$$A_{2,4} = \frac{\lambda}{2 \sqrt{n_1^2 - n_{2,4}^2}} \quad 1/2$$

Use the new symbols, Eqs. A26 and A27 become

$$k_x a = p\pi - \tan^{-1} \left( \frac{n_3^2}{n_1^2} \xi_3 k_x \right) - \tan^{-1} \left( \frac{n_5^2}{n_1^2} \xi_5 k_x \right) \quad A28a$$

$$k_y b = q\pi - \tan^{-1} (n_2 k_y) - \tan^{-1} (n_4 k_y) . \quad A28b$$

Eqs. A28a and A28b are the characteristic equations of the channel waveguide that can be solved numerically in general.

2.  $E_{pq}^y$  Modes: Polarization Along y

The field components are

$$H_{xv} = e^{i(\omega t - k_z z)} \left\{ \begin{array}{ll} M_1 \cos(k_x x + \alpha) \cos(k_y y + \beta) & v = 1 \\ M_2 \cos(k_x x + \alpha) e^{-k_y y} & v = 2 \\ M_3 \cos(k_y y + \beta) e^{-k_x x} & v = 3 \\ M_4 \cos(k_x x + \alpha) e^{-k_y y} & v = 4 \\ M_5 \cos(k_y y + \beta) e^{-k_x x} & v = 5 \end{array} \right.$$

$$H_{yv} = 0$$

$$H_{zv} = -\frac{i}{k_z} \frac{\partial H_x}{\partial x}$$

$$E_{xv} = 0$$

$$E_{yv} = \frac{1}{\omega \epsilon n_v^2 k_z} \left( k_x^2 n_v^2 - \frac{\partial^2}{\partial y^2} \right) H_{xv}$$

$$E_{zv} = \frac{i}{\omega \epsilon n_v^2} \frac{\partial H_{xv}}{\partial y}$$

We can carry out the analysis parallel to that of  $E_{pq}^x$  modes to obtain the characteristic equations as

$$k_x a = p\pi - \tan^{-1}(k_x \xi_3) - \tan^{-1}(k_x \xi_5)$$

$$k_y b = q\pi - \tan^{-1}\left(\frac{n_2^2}{n_1^2} k_y n_2\right) - \tan^{-1}\left(\frac{n_4^2}{n_1^2} k_y n_4\right)$$

### 3. Overlap Integrals

We have written computer programs which solve the above equations for the mode profiles. In our case, the  $\alpha$  of equation A15 is zero due to symmetry and all  $y$  dependencies can be ignored ( $y = 0$ ). Further, since all of our present devices primarily work for a single TE mode, we consider only the  $E_{00}^x$  case.

For the case of an angular bend, the coordinate transformation given by Eqs. A7 and A8 apply; we then have

$$\psi_1 = \begin{pmatrix} M_1 \cos(k_x x) \\ M_3 e^{-kx_3 x} \\ M_5 e^{-kx_5 x} \end{pmatrix} \quad \psi_2 = e^{-i k \sin \theta x} \begin{cases} M_1^1 \cos(k_x x \cos \theta) & v=1 \\ M_3^1 e^{-kx_3 x \cos \theta} & v=3 \\ M_5^1 e^{-kx_5 x \cos \theta} & v=5 \end{cases}$$

where  $M_1/M_3$  and  $M_1/M_5$  are given by Eq. A20. Eq. A2 can then be written as

$$= \frac{\left| \int_{-\infty}^{-a/2} \psi_{15}^* \psi_{25} dx + \int_{-a/2}^{+a/2} \psi_{11}^* \psi_{21} dx + \int_{a/2}^{\infty} \psi_{13}^* \psi_{23} dx \right|^2}{4 \left( \int_0^{a/2} \psi_{11}^* \psi_{11} dx + \int_{a/2}^{\infty} \psi_{13}^* \psi_{13} dx \right)^2}$$

where the second subscript refers to the region,  $v$ . These integrals have been performed in closed form, programmed and calculated. Results were presented earlier. (See Figure 22.)

For the displacement we have

$$\psi_1 = \begin{pmatrix} M_1 \cos(k_x x) \\ M_3 e^{-kx_3 x} \\ M_5 e^{-kx_5 x} \end{pmatrix} \quad \psi_2 = \begin{pmatrix} M_1 \cos(k_x(x-\delta)) \\ M_3 e^{-kx_3(x-\delta)} \\ M_4 e^{-kx_5(x-\delta)} \end{pmatrix}$$

The overlap integrals can be written

$$= \frac{\left| \int_{-a/2}^{-a/2+\delta} \psi_{15}^* \psi_{25} dx + \int_{-a/2+\delta}^{-a/2+\delta} \psi_{11}^* \psi_{25} dx + \int_{-a/2+\delta}^{a/2} \psi_{11}^* \psi_{21} dx + \int_{a/2}^{a/2+\delta} \psi_{13}^* \psi_{21} dx + \int_{a/2+\delta}^a \psi_{13}^* \psi_{23} dx \right|^2}{4 \left| \int_0^{a/2} \psi_{11}^* \psi_{11} dx + \int_{a/2}^a \psi_{13}^* \psi_{13} dx \right|^2}$$

These integrals have also been performed in closed form, programmed, and calculated. Results were presented earlier in Figure 23.

$$= \frac{\left| \int_{-a/2}^{-a/2+\delta} \psi_{15}^* \psi_{25} dx + \int_{-a/2+\delta}^{-a/2+\delta} \psi_{11}^* \psi_{25} dx + \int_{-a/2+\delta}^{a/2} \psi_{11}^* \psi_{21} dx + \int_{a/2}^{a/2+\delta} \psi_{13}^* \psi_{21} dx + \int_{a/2+\delta}^a \psi_{13}^* \psi_{23} dx \right|^2}{4 \left| \int_0^{a/2} \psi_{11}^* \psi_{11} dx + \int_{a/2}^a \psi_{13}^* \psi_{13} dx \right|^2}$$

DATE  
FILMED  
— 8